Establishing synthetic ribbon-type active zones in a heterologous expression system

Rohan Kapoor[1,2,3,8], Thanh Thao Do[4], Niko Schwenzer[5,6,8], Arsen Petrovic[4,8], Thomas Dresbach[7], Stephan E. Lehnart[5,6,8], Rubén Fernández-Busnadiego[4,8], Tobias Moser[1,2,3,8]

[1]Institute for Auditory Neuroscience and InnerEarLab, University Medical Center Göttingen, Germany.

[2]Auditory Neuroscience and Synaptic Nanophysiology Group, Max-Planck-Institute for Multidisciplinary Sciences, Göttingen, Germany.

[3]IMPRS Molecular Biology, Göttingen Graduate School for Neuroscience and Molecular Biosciences, University of Göttingen, Göttingen, Germany

[4]Institute for Neuropathology, University Medical Centre Göttingen, Göttingen, 37077, Germany

[5]Department of Cardiology and Pneumology, University Medical Center Göttingen; Göttingen, Germany

[6]Cellular Biophysics & Translational Cardiology Section, Heart Research Center Göttingen, University Medical Center Göttingen, Germany

[7]Institute of Anatomy and Embryology, University Medical Center Göttingen; Göttingen, Germany

[8]Cluster of Excellence "Multiscale Bioimaging: from Molecular Machines to Networks of Excitable Cells" (MBExC 2067), University of Göttingen, Germany

Correspondence: tmoser@gwdg.de

Abstract

Encoding of several sensory modalities into neural signals is mediated by ribbon synapses. The synaptic ribbon tethers synaptic vesicles at the presynaptic active zone (AZ) and may act as a super-scaffold organizing AZ topography. Here we employed a synthetic biology approach to reconstitute structures mimicking ribbon-type AZs in HEK293 cells for probing minimal molecular requirements and studying presynaptic Ca^{2+} channel clustering. Co-expressing a membrane-targeted version of the AZ-protein Bassoon and the ribbon core protein RIBEYE, we observed structures recapitulating basic aspects of ribbon-type AZs, which we call *synthetic* ribbons or *SyRibbons*. Super-resolution STED microscopy and cryo-correlative electron tomography revealed *SyRibbons* were similar to native ribbons at AZs of cochlear inner hair cells in shape and size. *SyRibbons* with Ca^{2+} channel clusters formed upon additional expression of $Ca_V1.3$ Ca^{2+} channels and RIM-binding protein 2 (RBP2). $Ca_V1.3$ Ca^{2+} channel clusters associated with *SyRibbons* were larger than ribbonless $Ca_V1.3$ Ca^{2+} channels clusters and functional analysis by Ca^{2+}-imaging in combination with patch clamp showed partial confinement of the Ca^{2+} signal at *SyRibbons*. In summary, we identify Ca^{2+} channels, RBP, membrane-anchored Bassoon, and RIBEYE as minimal components for reconstituting a basic ribbon-type AZ. *SyRibbons* might complement animal studies on molecular interactions of AZ proteins.

Keywords: calcium channel/channel cluster/calcium signal/ribbon synapse/synthetic biology

Significance Statement

Encoding of sensory information in our eyes and ears builds on specialized ribbon synapses of sensory cells. Elucidating the molecular underpinning of their fascinating structure and function is an ongoing effort to which we add a bottom-up reconstitution approach in cultured cells. Aiming to recapitulate basic properties of ribbon-type presynaptic active zones of cochlear inner hair cells, we identified a minimal set of proteins that assemble in cellular nanodomains, structurally and functionally alike active zones. While not yet reconstituting synaptic vesicle exocytosis, we consider the established synthetic ribbon-type active zones a valuable platform for studying molecular interactions of active zone proteins. We expect the approach to complement and reduce experiments on native ribbon synapses asserted from animals.

Introduction

Synapses of sensory receptor cells of the inner ear and the retina are hallmarked by the presence of an electron-dense structure called the synaptic ribbon, which tethers synaptic vesicles (SVs) at the presynaptic active zone (AZ, [Moser *et al*, 2019; Matthews & Fuchs, 2010]). Proposed functional roles

57 of the ribbon include (i) its role as a SV replenishment machine for tireless neurotransmission (Bunt,
58 1971; Holt *et al*, 2004; Khimich *et al*, 2005; Frank *et al*, 2010; Snellman *et al*, 2011; Graydon *et al*, 2011;
59 Vaithianathan *et al*, 2016), (ii) "super-scaffold" regulating the abundance, topography, and function of
60 AZ players such Ca^{2+} channels and release sites and their tight coupling (Khimich *et al*, 2005; Frank *et*
61 *al*, 2010; Wong *et al*, 2014; Maxeiner *et al*, 2016; Jean *et al*, 2018; Grabner & Moser, 2021), and iii)
62 coordination of SV release (Heidelberger *et al*, 1994; Glowatzki & Fuchs, 2002; Singer *et al*, 2004;
63 Edmonds, 2004; Mehta *et al*, 2013). Yet, our molecular understanding of how these postulated
64 functions are executed by synaptic ribbons is still limited.

65 Likewise, the clustering of Ca^{2+} channels at the AZ, how it is varied among different or even the
66 same synapse types and how the ribbon contributes towards this, remain active areas of research
67 (Wichmann & Kuner, 2022; Moser *et al*, 2023). For example, ribbon synapses of mature inner hair cells
68 (IHC) assemble $Ca_V1.3$ voltage-gated Ca^{2+} channels at the base of the ribbon, but vary in shape, size
69 and channel complement of the $Ca_V1.3$ clusters (Frank *et al*, 2010; Wong *et al*, 2014; Neef *et al*, 2018)
70 partially dependent on the position within the IHC (Ohn *et al*, 2016; Özçete & Moser, 2021). IHC
71 synapses lacking AZ-anchored ribbons in Bassoon mutant mice showed fewer Ca^{2+} channels with
72 altered topography (Frank *et al*, 2010; Neef *et al*, 2018). While genetic disruption of Ca^{2+} channel-
73 tethering AZ proteins RIM2 (Jung *et al*, 2015) and RBP2 (Krinner *et al*, 2017) reduced the abundance of
74 Ca^{2+} channels at IHC synapses, their topography retained the typical stripe-like shape of Ca^{2+} channel
75 clusters. Constitutive deletion of RIBEYE, the core scaffold protein of the synaptic ribbon, provided so
76 far the most direct test of the scaffolding role of the ribbon (Maxeiner *et al*, 2016; Jean *et al*, 2018;
77 Becker *et al*, 2018; Grabner & Moser, 2021). Here, ribbon-less synapses of IHCs showed an altered Ca^{2+}
78 channel topography with a more spatially widespread presynaptic Ca^{2+} signal but intact Ca^{2+} channel
79 complement (Jean *et al*, 2018). Moreover, the voltage-dependence of activation as well as the
80 inactivation of Ca^{2+} channels appeared to be altered, suggesting a possible role of the synaptic ribbon
81 in regulating Ca^{2+} channel physiology (Jean *et al*, 2018). Changes in Ca^{2+} channel physiology upon
82 deletion of RIBEYE were also found for $Ca_V1.4$ at ribbon-less rod photoreceptor AZs (Grabner & Moser,
83 2021). Finally, IHCs lacking piccolino, a ribbon-synapse specific isoform of the AZ protein piccolo, show
84 AZs with smaller synaptic ribbons and altered clustering, yet normal complement of Ca^{2+} channels
85 (Michanski *et al*, 2023).

86 So how does the synaptic ribbon tune into the orchestra of AZ proteins that collectively
87 organize Ca^{2+} channel abundance, topography, and function? To what extent can the effects observed
88 upon disruption of Bassoon be attributed to the concomitant loss of the ribbon? These questions seem
89 even more relevant given that, so far to our knowledge, no direct interactions between Bassoon (Frank
90 *et al*, 2010) or RIBEYE and $Ca_V1.3$ Ca^{2+} channel have been described. Here, we adopted a bottom-up
91 synthetic biology approach to assemble a minimal presynaptic protein machinery required to bring

92 together RIBEYE and Ca^{2+} channels in a 'synapse-naïve' expression system to assess the role of the
93 synaptic ribbon in regulating Ca^{2+} channel clustering and physiology. Similar approaches have
94 previously been employed for reconstituting aspects of conventional synapses, for instance in "hemi-
95 synapses" between co-cultured neurons and non-neuronal cells overexpressing presynaptic or
96 postsynaptic components (for review see Craig *et al*, 2006). More recently, Munc13-1 supra-molecular
97 assemblies which recruit release machinery proteins were reconstituted (Sakamoto *et al*, 2018).
98 Expression of RIBEYE in synapse-naïve cell lines such as COS-7 cells led to large cytosolic
99 assemblies (Schmitz *et al*, 2000). Ribbon-like electron dense structures with vesicles have also been
100 reported upon heterologous RIBEYE expression in retinal progenitor cell-line (R28, [Magupalli *et al*,
101 2008]). However, these cells might not be considered synapse-naïve and the presence and function of
102 Ca^{2+} channels at synthetic ribbon synapses remained to be studied. The need for co-expressing at least
103 three Ca^{2+} channel subunits ($Ca_V\alpha_x$, $Ca_V\beta_x$ and $Ca_V\alpha_2\delta_x$) in synapse-naïve cell lines renders acute co-
104 expression of AZ multidomain proteins cumbersome. Here we took advantage of synapse-naïve
105 Human Embryonic Kidney 293 (HEK293) cells stably expressing inducible $Ca_V1.3\alpha_1$, which is the
106 predominant subtype of voltage-gated Ca^{2+} channels at IHC ribbon synapses (Brandt *et al*, 2003; Platzer
107 *et al*, 2000; Dou *et al*, 2004), as well as constitutively expressed $Ca_V\beta_3$ and $Ca_V\alpha_2\delta_1$. We co-expressed
108 RIBEYE along with membrane targeted Bassoon and observed structures with striking resemblance to
109 IHC synaptic ribbon-type AZs nicknamed '*SyRibbons*'. We characterized the structure and function of
110 these synthetic ribbon-type AZs and identified Bassoon, RBP2, RIBEYE and $Ca_V1.3$ channels as the
111 minimal components required for assembling a basic ribbon-type AZ. We observed larger $Ca_V1.3$
112 channel clusters near *SyRibbons* and with partially localized Ca^{2+} influx upon stimulation. Our results
113 support the role of synaptic ribbons in promoting the formation of $Ca_V1.3$ channel micro-clustering.
114 Synthetic ribbon-type AZs offer a novel approach for functionally studying protein-protein interaction
115 and will likely complement, refine and reduce experiments on native ribbon synapses.
116

117 ## Results

118 ### Membrane-targeted Bassoon recruits RIBEYE to the cell membrane in HEK293 cells where structures
119 mimicking inner hair cell synaptic ribbons are formed.

120 HEK293 cells have the advantage of not expressing the synaptic machinery components studied here.
121 This provides a clean background for reconstituting synthetic synapses from a minimal set of synaptic
122 proteins. Our first step towards assembling a ribbon-type AZ in a heterologous expression system was
123 to express RIBEYE, the core scaffold protein of the synaptic ribbon, and target it to the cell membrane.
124 We performed transient transfection of a RIBEYE construct with a C-terminal EGFP tag in HEK293 cells
125 and observed large spherical clusters of RIBEYE that appeared largely cytosolic (Fig. 1Aii), in contrast
126 to a diffuse cytosolic distribution when merely expressing EGFP (Fig. 1Ai). These RIBEYE clusters form

127 due to self-assembling properties of RIBEYE via multiple sites of homophilic interaction as have been
128 demonstrated before in several cell lines. They do not colocalize with the endoplasmic reticulum (ER),
129 Golgi apparatus, or lysosomes and hence, are unlikely to reflect RIBEYE entrapped in protein trafficking
130 pathways or to represent degradation products of overexpressed RIBEYE (Supplementary Fig. 1A, B
131 and C).

132 Next, for membrane targeting of these cytosolic RIBEYE clusters, we co-expressed the multidomain
133 cytomatrix of the active zone protein Bassoon (Fig. 1Aiii). Prior work on the molecular underpinnings
134 of ribbon synapses had identified Bassoon (tom Dieck *et al*, 1998) to critically contribute to anchoring
135 the synaptic ribbon to the AZ membrane (Khimich *et al*, 2005; Dick *et al*, 2003; tom Dieck *et al*, 2005).
136 Co-expression of full-length Bassoon along with RIBEYE in HEK293 cells showed colocalizing clusters of
137 the two proteins that, however, remained largely cytosolic (Fig. 1Aiv).

138 Next, for plasma membrane-targeting of Bassoon, we generated a construct by removing the first 95
139 N-terminal amino acids of Bassoon and replacing these with a palmitoylation consensus sequence of
140 the neuronal Growth Associated Protein 43 (GAP43). We refer to this as 'palm-Bassoon' throughout,
141 and we used constructs with and without a C-terminal EGFP tag (Fig. 1B). Expression of either of these
142 palm-Bassoon constructs in HEK293 cells showed comparable immunofluorescence patterns with
143 Bassoon puncta spread across the periphery of the cell, largely colocalizing with the endogenously
144 expressed plasma membrane-standing Na, K-ATPase α_1 (data representative of 3 transfections, Fig. 1C,
145 D). Palm-Bassoon does not appear to localize in the ER, Golgi apparatus or lysosomes (Supplementary
146 Fig. 1D, E and F). Comparing the ratio of Bassoon signal intensity at the periphery *versus* inside of the
147 cell in randomly selected single sections from confocal stacks of palm-Bassoon and Bassoon
148 transfected cells (N = 10 cells, 3 transfections per group, Fig. 1E) demonstrated a higher Bassoon signal
149 intensity at the periphery of cells expressing the palm-Bassoon construct (****P < 0.0001, Mann-
150 Whitney-Wilcoxon test), implying successful plasma membrane targeting of Bassoon.

151

152

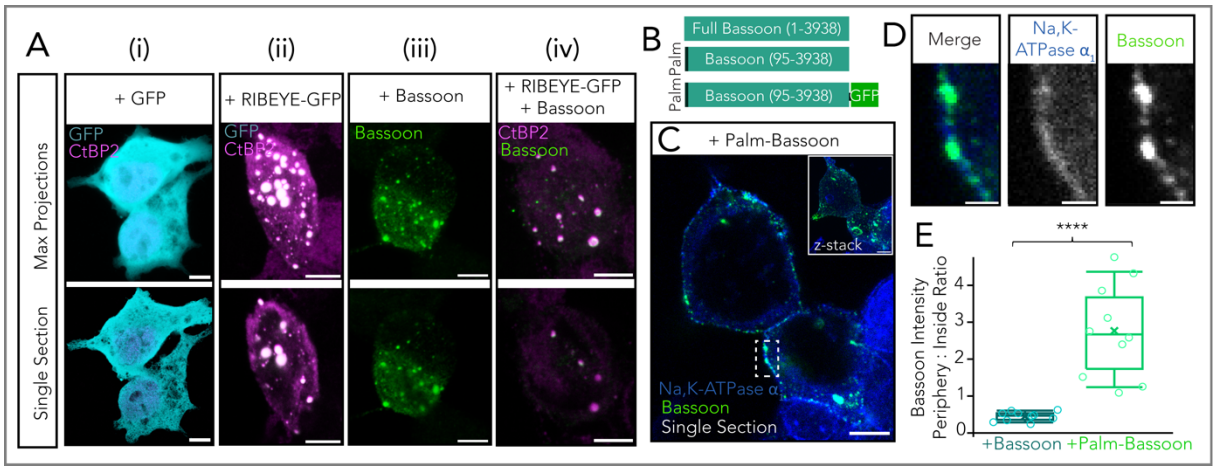

153

154 **Figure 1 - Membrane targeting of Bassoon using a palmitoylation consensus sequence.**

155 **A** Representative confocal images of HEK293 cells transfected with (i) GFP only (CtBP2/RIBEYE in
156 magenta labeling nuclei, GFP in cyan), (ii) RIBEYE-GFP (CtBP2/RIBEYE in magenta, GFP in cyan), (iii)
157 Bassoon (green) and (iv) RIBEYE-GFP and Bassoon. Note that antibodies against RIBEYE B-domain
158 and the nuclear transcription factor CtBP2 result in similar staining patterns as CtBP2 is transcribed
159 from the same gene as RIBEYE and is identical to the RIBEYE-B domain except for the first 20 N-
160 terminal amino acids. Upper panel shows maximum projections and lower panel shows exemplary
161 single sections from confocal stacks. Scale bar = 5 µm.

162 **B** Schematic of construct for membrane targeting of Bassoon. The first 95 amino acids from full-
163 length Bassoon were replaced with a palmitoylation consensus sequence from GAP43. Constructs
164 without and with a C-terminal GFP tag were used, as depicted.

165 **C** Sample confocal image (single section) showing membrane targeted palm-Bassoon (green)
166 expressed in HEK293 cells appears as puncta distributed along the periphery of the cell, marked
167 by Na, K-ATPase α_1(blue). Inset shows maximal projection of confocal section. Scale bar = 5µm.

168 **D** Zoom-in from **(C)** shows colocalisation of palm-Bassoon with membrane marker Na, K-ATPase α1.
169 Scale bar = 1µm.

170 **E** Quantification of Bassoon signal intensity at periphery *vs* inside of cell. Cells expressing palm-
171 Bassoon (N = 10 cells) clearly show a higher peripheral distribution compared to cells expressing
172 full-length Bassoon (N = 10 cells), ****P < 0.0001, Mann-Whitney-Wilcoxon test. Overlaid data
173 points represent individual cells, crosses represent the mean values, central band indicates the
174 median, whiskers represent 90/10 percentiles, and boxes represent 75/25 percentiles.

175

176 Next, we co-expressed palm-Bassoon and RIBEYE in HEK293 cells and observed colocalizing RIBEYE and
177 Bassoon immunofluorescent puncta at the periphery of cells (7 transfections; Fig. 2Ai). Closer
178 inspection of these immunofluorescent puncta with STimulated Emission Depletion (STED) nanoscopy
179 (Fig. 2Aii) revealed discrete structures typically consisting of ellipsoidal RIBEYE clusters juxtaposing on
180 top of plate-like palm-Bassoon structures which seemingly anchor the RIBEYE clusters to the plasma
181 membrane. We found the morphology of the RIBEYE + palm-Bassoon structures to be strikingly
182 reminiscent of the arrangement of the two proteins in IHC ribbon synapses, where an
183 ellipsoid/spherical synaptic ribbon composed of RIBEYE is found seated on a Bassoon plate that

184 anchors it to the presynaptic AZ membrane (e.g. Wong *et al*, 2014; Michanski *et al*, 2019, 2023) (Fig.
185 2B, i and ii; data from Michanski *et al*, 2023).
186 We compared the RIBEYE and Bassoon signal intensities at the periphery *versus* inside of the
187 cell in randomly selected single sections from confocal stacks of HEK cells expressing RIBEYE and palm-
188 Bassoon (N = 9 cells) and HEK cells expressing RIBEYE and full-length Bassoon (N=9 cells). We found an
189 increased peripheral distribution of both RIBEYE and Bassoon when using palm-Bassoon (Fig. 2C, ****P
190 < 0.0001, Mann-Whitney-Wilcoxon test), implying successful membrane targeting of RIBEYE by palm-
191 Bassoon. In each transfection, ~10% cells showed co-expression of both RIBEYE and palm-Bassoon (for
192 representative sample overview see Supplementary Fig. 2). Of those, cells expressing discrete RIBEYE-
193 palm Bassoon structures were discernible by the characteristic RIBEYE distribution along the periphery
194 of the cell. This peripheral distribution in turn seemingly depends upon RIBEYE and palm-Bassoon
195 expression ratios (shown in Supplementary Fig. 2B) as cells with little to no palm-Bassoon expression
196 show predominantly cytosolic RIBEYE puncta and were not used for analysis. For simplicity, we
197 henceforth refer to the structures composed of RIBEYE and palm-Bassoon in HEK293 cells as *SyRibbons*
198 (for *synthetic* ribbons).
199
200 We next performed three-dimensional surface renderings using *Imaris* 9.6 (Oxford Instruments) to
201 assess these structures. In a given cell, only structures with colocalizing RIBEYE and palm-Bassoon
202 immunofluorescence were considered for analysis to exclude occasional non-membrane localized
203 spots (on average 51.75 ± 40.84 RIBEYE surfaces colocalizing with Bassoon surfaces per cell; N = 20
204 cells). The volumes of RIBEYE and palm-Bassoon surfaces of *SyRibbons* were smaller on average and
205 more variable (average volume ± standard deviation (SD) = 0.19 ± 0.23 μm^3 with a coefficient of
206 variation (CV) = 1.23 for RIBEYE; n_{spots} = 864 and volume = 0.17 ± 0.18 μm^3 with CV = 1.10 for Bassoon;
207 n_{spots} = 951; data from N = 20 cells, quantifications from 5 sample transfections) than volumes of
208 synaptic ribbons and Bassoon immunofluorescent puncta from rat IHCs (volume = 0.29 ± 0.17 μm^3, CV
209 = 0.59 for RIBEYE; n_{spots} = 290, and volume = 0.27 ± 0.18 μm^3, CV = 0.67 for Bassoon; n_{spots} = 314, data
210 from N = 29 cells), (Fig. 2D, E). Moreover, volumes of RIBEYE surfaces show a high positive correlation
211 to volumes of corresponding palm-Bassoon surfaces (P_r = 0.778, ****P < 0.0001), implying that larger
212 palm-Bassoon structures may recruit bigger RIBEYE structures to the plasma membrane. We also note
213 that the volume of RIBEYE surfaces in *SyRibbons* appears smaller and well-regulated in contrast to the
214 predominantly large, cytosolic RIBEYE assemblies in cells co-expressing RIBEYE and full-length Bassoon
215 (volume = 0.30 ± 0.36 μm^3, n_{spots} = 460, N = 10 cells, ****P < 0.001, Mann-Whitney-Wilcoxon Test). In
216 turn, Bassoon clusters seemed regulated by co-expressed RIBEYE: Bassoon surfaces at the plasma
217 membrane were larger at *SyRibbons* than in the absence of RIBEYE in cells only expressing palm-
218 Bassoon (volume = 0.14 ± 0.21 μm^3, n_{spots} = 2217, N = 13 cells, ****P < 0.001, Mann-Whitney-Wilcoxon

Test). RIBEYE clusters constituting *SyRibbons* appeared more spherical than the plate-like Bassoon structures in the same cells (sphericity Ψ = 0.91 ± 0.05, n_{spots} = 864 for RIBEYE versus Ψ = 0.86 ± 0.07, n_{spots}= 951 for Bassoon, data from N = 20 cells; ****P < 0.0001, Kruskal-Wallis test with *post hoc* Dunn's multiple comparison test). This follows the same trend as in rat IHCs where RIBEYE spots indeed appear more spherical (Ψ = 0.90 ± 0.05, n_{spots} = 290) compared to Bassoon spots (Ψ = 0.76 ± 0.10, n_{spots} = 314); ****P < 0.0001, Kruskal-Wallis test with *post hoc* Dunn's multiple comparison test, data from N = 29 cells (Fig. 2F). Nonetheless, the fact that next to structures with volumes comparable to IHC ribbons, we also encountered smaller and larger structures, likely reflects poorer regulation of RIBEYE and palm-Bassoon expression in the heterologous system.

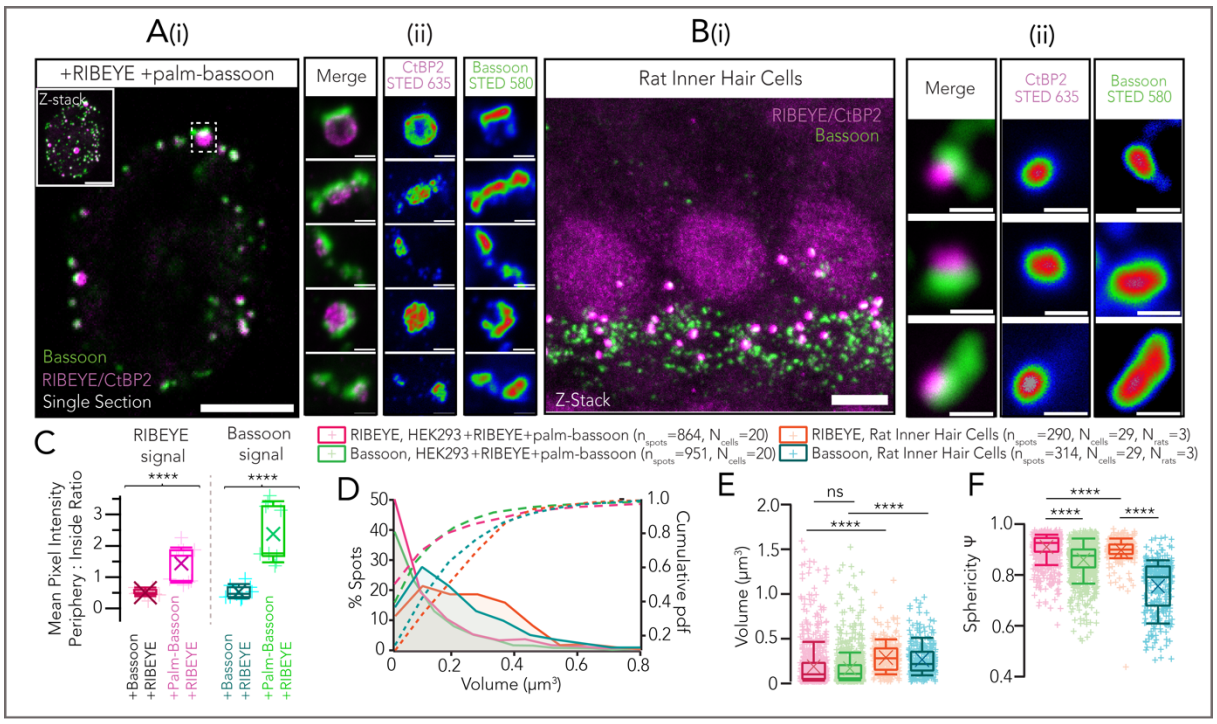

Figure 2 - Co-expression of RIBEYE with palm-Bassoon results in ribbon-type AZ-like structures

A (i) Representative confocal image (single section) of a HEK293 cell transfected with RIBEYE-GFP (magenta) and palm-Bassoon (green). Co-expression of RIBEYE with palm-Bassoon targets RIBEYE to the cell membrane. Inset shows maximum projection. Scale bar = 5µm. (ii) Exemplary 2-D STED images for RIBEYE – palm-Bassoon juxtapositions acquired from cells as shown in (i); Scale bar = 500nm; individual channels have been depicted with an intensity-coded look-up table with warmer colors indicating higher intensity.

B **(i)** Representative maximum projection of confocal sections of apical organ of Corti from a Wistar rat (postnatal day 18); data as published in Michanski *et al*, 2023, stainings were for CtBP2/RIBEYE (magenta; labeling synaptic ribbons and IHC nuclei) and Bassoon (green; spots juxtaposing with ribbons represent IHC AZs, spots not juxtaposing with ribbons represent efferent synapses formed by lateral olivocochlear neurons onto SGN boutons). Scale bar = 5µm. **(ii)** Juxtaposing RIBEYE and Bassoon spots imaged in 2-D STED and confocal mode respectively. Scale bar = 500nm. Note the striking resemblance to reconstituted RIBEYE + palm-Bassoon structures in HEK293 cells as shown in **(Aii)**. STED images are from 3 sample transfections, representative of 7 total transfections;

245 individual channels have been depicted with an intensity-coded look-up table with warmer colors
246 indicating higher intensity.

247 **C** Quantification of RIBEYE and Bassoon signal intensity at periphery *vs* inside of cell shows a higher
248 peripheral distribution of RIBEYE and Bassoon in HEK293 + RIBEYE + palm-Bassoon cells (N=9 cells)
249 as compared to HEK293 + RIBEYE + Bassoon cells (N=9 cells); *****P* < 0.0001, Mann-Whitney-
250 Wilcoxon test. Overlaid data points represent individual cells, crosses represent mean values,
251 central band indicates the median, whiskers represent 90/10 percentiles, and boxes represent
252 75/25 percentiles.

253 **D** Distribution of volumes of RIBEYE and palm-Bassoon puncta from HEK293 cells expressing RIBEYE
254 and palm-Bassoon (n = 20 cells, quantifications from 5 sample transfections). Volumes of synaptic
255 ribbons from rat IHCs (n = 29 cells, 3 rats) have been plotted for comparison.

256 **E** Box plot depicting data from **(D)**. Volumes of RIBEYE and palm-Bassoon puncta are comparable to
257 each other (*P* > 0.99, Kruskal-Wallis test with *post hoc* Dunn's multi-comparison), but on an
258 average much smaller and considerably more variable when compared to volumes of RIBEYE and
259 Bassoon puncta from rat IHCs respectively (*****P* < 0.0001, Kruskal-Wallis test with *post hoc*
260 Dunn's multi-comparison). Overlaid plus signs represent individual spots, crosses represent mean
261 values, central band indicates the median, whiskers represent 90/10 percentiles and boxes
262 represent 75/25 percentiles.

263 **F** RIBEYE puncta in HEK cells expressing RIBEYE and palm-Bassoon (n_{spots} = 864, N = 20 cells) appear
264 more spherical than Bassoon puncta in the same cells (n_{spots} = 961, N = 20 cells; *****P* < 0.0001,
265 Kruskal-Wallis test with *post hoc* Dunn's multiple comparison test). Note the similar trend in IHC
266 synaptic ribbons where RIBEYE puncta are more spherical than Bassoon puncta (n_{spots} = 290 for
267 RIBEYE and n_{spots} = 314 for Bassoon, N = 29 cells, 3 rats; *****P* < 0.0001, Kruskal-Wallis test with
268 *post hoc* Dunn's multiple comparison test). Overlaid plus signs represent individual spots, crosses
269 represent mean values, central band indicates the median, whiskers represent 90/10 percentiles
270 and boxes represent 75/25 percentiles.

271

272 Next, we analyzed *SyRibbons* in situ using cryo-electron tomography (cryo-ET), which capitalizes on cell
273 vitrification to obtain near-native preservation. Plunge-frozen HEK cells transfected with RIBEYE-GFP
274 and untagged palm-Bassoon were vitrified and subsequently milled using a cryo-focused ion beam
275 (cryo-FIB; Supplementary Fig. 3A) to produce 150 nm-thick lamellae as previously described (Rigort *et*
276 *al*, 2010; Pierson *et al*, 2024, see methods). Using a light microscope integrated in the cryo-FIB
277 chamber, we targeted cell areas showing peripheral GFP fluorescence corresponding to *SyRibbons*
278 (Supplementary Fig. 3B). Lamellae were subsequently transferred to a cryo-transmission electron
279 microscope, and tomographic tilt-series were acquired at fluorescence locations. The tomograms
280 showed that GFP-positive RIBEYE spots corresponded to electron-dense structures (Fig 3A-B), as is
281 characteristic of the synaptic ribbon (Robertis & Franchi, 1956; Smith & Sjöstrand, 1961). These
282 electron-dense *SyRibbons* appeared to be approx. 300 – 800 nm in size and were ovoid or ellipsoidal
283 in shape (Fig 3B-C, Supplementary Fig. 3C). Some *SyRibbons* displayed a hollow core (Supplementary
284 Fig. $3C_i$ and $3C_{iii}$) and on closer inspection, some appeared to have a multi-lamellar ultrastructure
285 (Supplementary Fig. $3C_{ii}$), both of which have been reported previously for natively expressed synaptic
286 ribbons in the inner ear and the retina (Michanski *et al*, 2023, 2019; Sobkowicz *et al*, 1982; Liberman,
287 1980; Stamataki *et al*, 2006; Wichmann & Moser, 2015). We captured a *SyRibbon* positioned within

288 100 nm from the plasma membrane (Fig 3C). Although bona fide ribbons display a halo of SVs tethered
289 on their surface, we did not observe any obvious accumulation of vesicular structures around these
290 *SyRibbons*, which is not unexpected for synapse-naïve HEK cells. This is in contrast to a previous report
291 in R28 retinal progenitor cells, where heterologously expressed RIBEYE was shown to recruit vesicles
292 (Magupalli *et al*, 2008). Intriguingly, in some tomograms, we observed membrane-bound *SyRibbons*
293 (Supplementary Fig. $3C_{i\text{-}iv}$), which may indicate an autophagic engulfment of some of these
294 overexpressed structures.

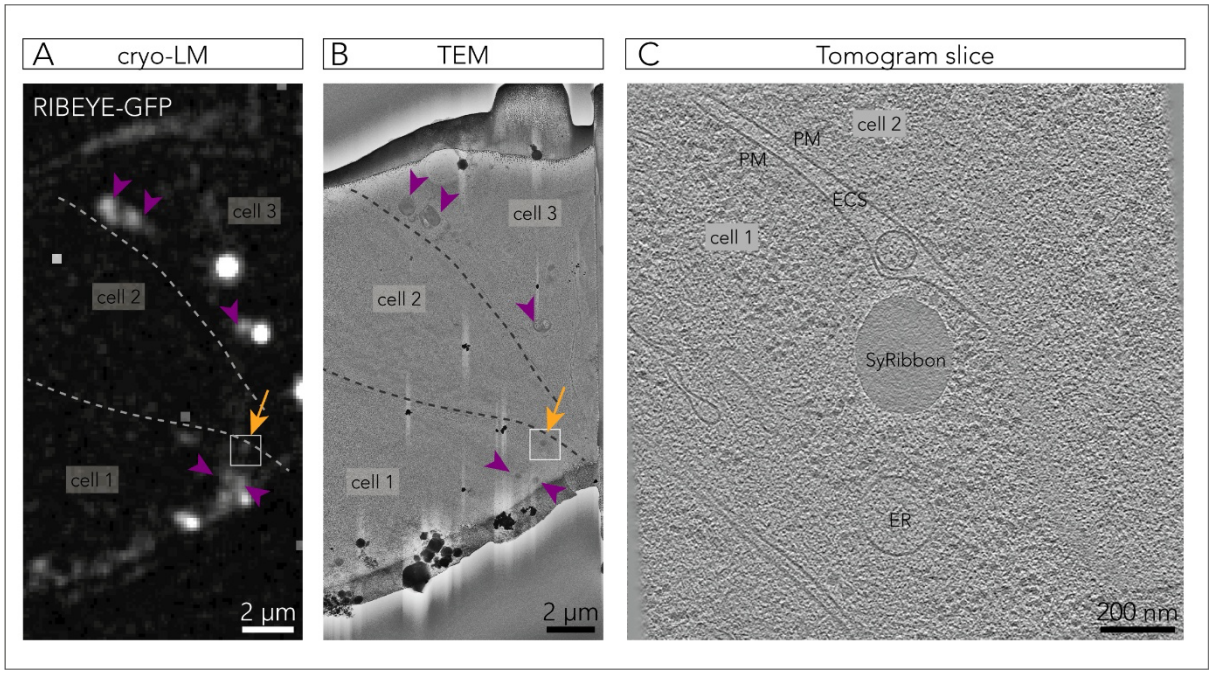

295

296 **Figure 3 - Cryo-correlative microscopy captures membrane-localised *SyRibbons*.**

297 **A**. RIBEYE-GFP signal on a 150 nm thick lamella, revealed by fluorescent light microscopy within the
298 cryo-FIB chamber (cryo-LM). Dotted lines delineate cell membranes. The orange arrow indicates a
299 plasma membrane-proximal GFP fluorescence, whereas purple arrow heads point to cytosolic RIBEYE
300 aggregates. The tomogram shown in (C) was acquired at the boxed region. The image underwent
301 background subtraction for better visualization.

302 **B**. Transmission electron microscopy (TEM) image of the lamella in A. Orange arrow and purple
303 arrowheads locate the respective regions in (A), showing that GFP-positive spots correlated to electron
304 dense bodies. Dotted lines delineate plasma membranes. The tomogram shown in (C) was taken at the
305 boxed region.

306 **C**. Tomogram slice showing a *SyRibbon* acquired at the boxed region in (B). *PM*: plasma membrane,
307 *ECS*: extracellular space *ER*: endoplasmic reticulum.

308

309

310

311

312

313 **RBP2 tethers $Ca_V1.3$ channels.**

314 To study the potential of *SyRibbons* to cluster Ca^{2+} channels, we employed HEK293 cells stably
315 expressing an inducible transgene of $Ca_V1.3\alpha_1$ along with constitutive transgenes for $Ca_V\beta_3$ and
316 $Ca_V\alpha_2\delta_1$. We either used tetracycline for inducible $Ca_V1.3\alpha_1$ channel expression (Fig. 4A) or performed
317 transient transfections with $Ca_V1.3$ constructs containing an N-terminal EGFP- (Fig. 4B) or Halo-tag (Fig.
318 4C) for direct fluorescence imaging. Expression of either Ca^{2+} channel complex resulted in small clusters
319 at the plasma membrane as represented in Fig. 4D (average volume 0.08 ± 0.13 µm^3, n_{spots} = 949, N =
320 12 cells for untagged inducible $Ca_V1.3\alpha_1$; 0.07 ± 0.08 µm^3, n_{spots} = 392, N = 11 cells for EGFP-$Ca_V1.3$; and
321 0.07 ± 0.09 µm^3, n_{spots} = 1281, N = 16 cells for Halo-$Ca_V1.3\alpha$; $P_{untagged/EGFP}$ = 0.547, $P_{untagged/Halo}$ > 0.999,
322 $P_{Halo/EGFP}$ = 0.582, Kruskal-Wallis test with *post hoc* Dunn's multiple comparison test).

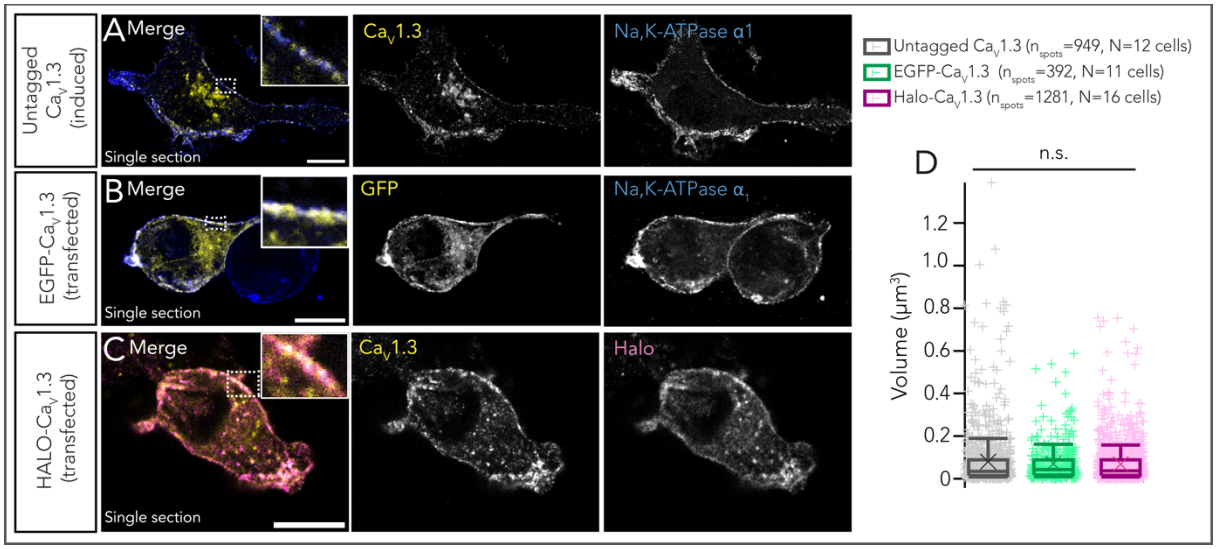

323

324 **Figure 4 - HEK293 cells expressing $Ca_V1.3$**

325 **A** Representative confocal section of a HEK293 cell stably expressing an inducible
326 $Ca_V1.3\alpha$ transgene (untagged) along with constitutive transgenes for $Ca_V\beta_3$ and $Ca_V\alpha_2\delta_1$.
327 Immunostainings have been performed using antibodies against $Ca_V1.3$ (green) and Na, K-
328 ATPase α_1 (blue, labeling the plasma membrane). Scale bar = 10 µm.

329 **B** Representative confocal section of a HEK293 cell stably expressing $Ca_V\beta_3$ and $Ca_V\alpha_2\delta_1$, and
330 transiently transfected with an N-terminal EGFP- tagged $Ca_V1.3$ construct. Immunostainings
331 have been performed using antibodies against GFP (green) and Na, K-ATPase α_1 (blue). Scale
332 bar = 10 µm.

333 **C** Representative confocal section of a HEK293 cell stably expressing $Ca_V\beta_3$ and $Ca_V\alpha_2\delta_1$ and
334 transiently transfected with an N-terminal Halo-tagged $Ca_V1.3$ construct. Immunostainings
335 have been performed using antibodies against $Ca_V1.3$ (green) and Halo tag (magenta). Scale
336 bar = 10 µm.

337 **D** Expression of either of the Ca^{2+} channel complexes result in clusters of comparable sizes, (P >
338 0.05, Kruskal-Wallis test with *post hoc* Dunn's multiple comparison test). Overlaid plus signs
339 represent individual spots, crosses represent mean values, central band indicates the median,
340 whiskers represent 90/10 percentiles and boxes represent 75/25 percentiles.

341

342 Co-expression of palm-Bassoon did not show colocalization with $Ca_V1.3$, which is in line with
343 observations with full-length Bassoon (Frank *et al*, 2010) and the same applied when co-expressing
344 RIBEYE and $Ca_V1.3$, arguing against a direct interaction for both (Supplementary Fig. 4). Rab-interacting
345 molecule-binding protein (RIM-BP or RBP) links Bassoon to Ca^{2+} channels (Davydova *et al*, 2014) and
346 hence was an interesting candidate for tethering $Ca_V1.3$ to Bassoon clusters. RBP has been shown to
347 interact with $Ca_V1.3$ (Hibino *et al*, 2002) and to be required for normal $Ca_V1.3$ Ca^{2+} channel clustering
348 at the IHC ribbon synapse (Krinner *et al*, 2017, 2021). Indeed, when co-expressing RBP2 with palm-
349 Bassoon and $Ca_V1.3$, we found juxtaposed palm-Bassoon and $Ca_V1.3$ both with immunolabeled (Fig.
350 5A) and live-labeled (Fig. 5B, C) proteins indicating successful clustering of $Ca_V1.3$ at *synthetic* AZs.

351 We next performed ruptured whole-cell patch-clamp to assess if RBP2 and/or palm-Bassoon or RIBEYE
352 co-expression results in changes in $Ca_V1.3$ Ca^{2+} currents. After tetracycline treatment for $Ca_V1.3\alpha_1$
353 expression (18-24 hours), cells were transfected with both RBP2-p2A-mKATE2 and palm-Bassoon-GFP,
354 with only palm-Bassoon-GFP, only RBP2-p2A-mKATE2 or RIBEYE-GFP constructs (Supplementary Fig.
355 5A). After 18-24 hours, the cell culture media was changed, and cells were recorded 24-36 hours
356 afterwards. We used 10 mM $[Ca^{2+}]_e$ and recorded Ca^{2+} current (density) - voltage relations (IVs) ~1
357 minute after establishing the whole-cell configuration by applying step depolarizations of 20 ms from
358 -86.2 mV to 58.8 mV in 5 mV increments. Ca^{2+} current density appeared to be augmented upon
359 expression of both RBP2 and palm-Bassoon when compared with induced-only controls
360 (Supplementary Fig. 5B, D; $^{**}P = 0.0041$, Kruskal-Wallis test with *post hoc* Dunn's multiple comparison
361 test). However, Ca^{2+} current density in cells expressing only RBP2 or Palm-Bassoon did not significantly
362 differ from either induced-only controls or cells expressing both proteins ($P > 0.05$, Kruskal-Wallis test
363 with *post hoc* Dunn's multiple comparison test). For cells expressing only RIBEYE, we also did not
364 observe any changes ($P > 0.999$, Kruskal-Wallis test with *post hoc* Dunn's multiple comparison test).
365 We did not observe any noticeable differences in voltage-dependence, activation kinetics or
366 inactivation kinetics of $Ca_V1.3$ Ca^{2+} current upon expression of any of these AZ proteins (Supplementary
367 Fig. 5C, E, F; Supplementary Fig. 6A, B).

368

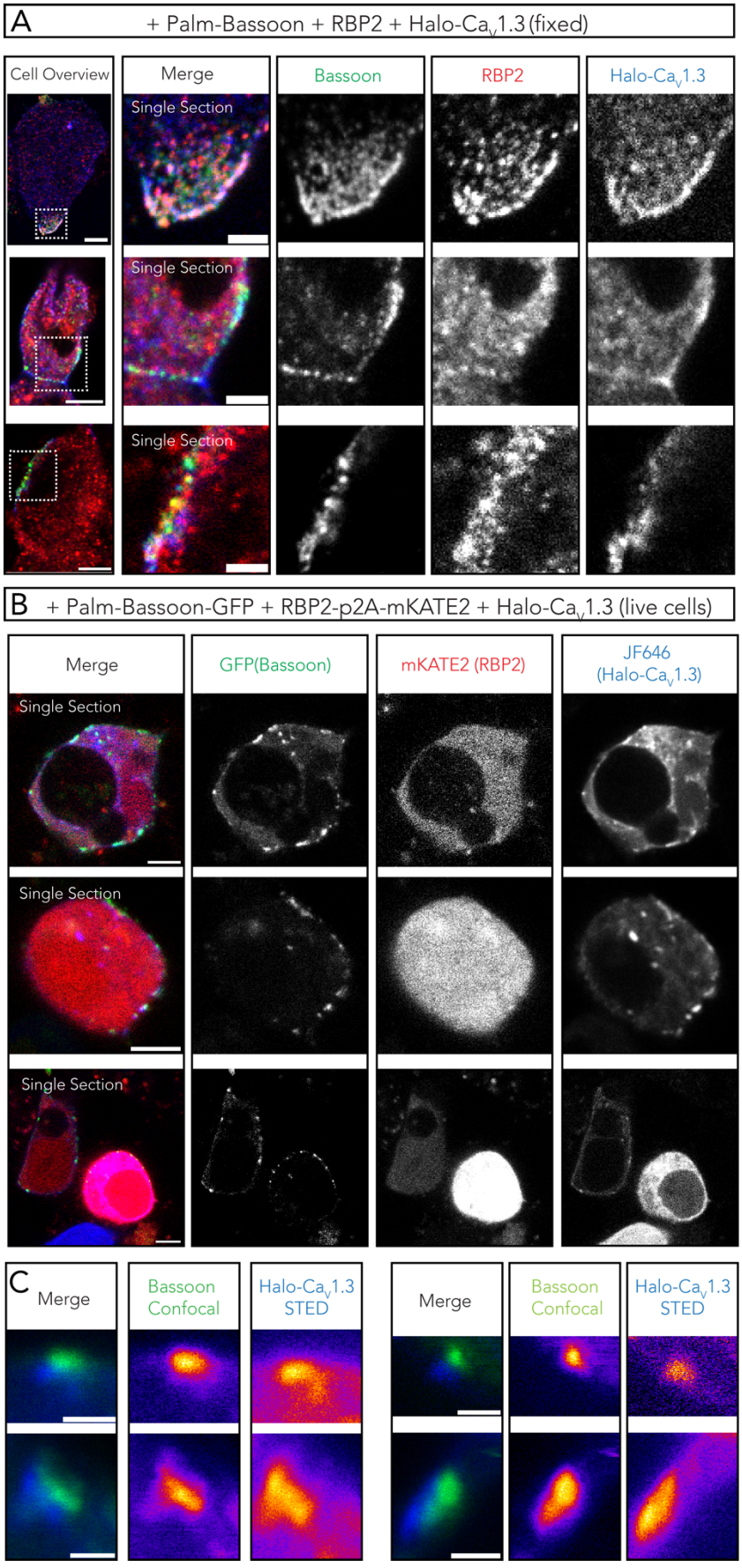
A
+ Palm-Bassoon + RBP2 + Halo-Ca$_V$1.3 (fixed)
Cell Overview
Merge
Bassoon
RBP2
Halo-Ca$_V$1.3
Single Section
Single Section
Single Section
B
+ Palm-Bassoon-GFP + RBP2-p2A-mKATE2 + Halo-Ca$_V$1.3 (live cells)
Merge
GFP(Bassoon)
mKATE2 (RBP2)
JF646
(Halo-Ca$_V$1.3)
Single Section
Single Section
Single Section
C
Merge
Bassoon
Confocal
Halo-Ca$_V$1.3
STED
Merge
Bassoon
Confocal
Halo-Ca$_V$1.3
STED

369

370 **Figure 5 – RBP2 bridges palm-Bassoon and $Ca_V1.3$ to form supra-molecular assemblies at the plasma**
371 **membrane.**

372 **A** Representative confocal images (single sections) of HEK293 cells (fixed) transfected with palm-
373 Bassoon (green), RBP2 (red) and N-terminal Halo-tagged $Ca_V1.3$ (blue). The three colocalizing
374 proteins appear to form supra-molecular assemblies at the cell membrane. Scale bar = 5 µm for
375 left panel showing cell overviews, 2 µm for right panels showing zoom-ins.

376 **B** Representative confocal images (single sections) of live HEK293 cells transfected with palm-
377 Bassoon-GFP (green), RBP2-p2A-mKATE2 (red, representing only mKATE2 signal and not RBP2
378 localization) and Halo-$Ca_V1.3$ (blue, labeled by with JF-646 HaloTag Ligand before imaging). Scale
379 bar = 5 µm.

380 **C** Exemplary super-resolution STED images from live-labeled samples in (B) showing juxtaposition
381 of palm-Bassoon and Halo-$Ca_V1.3$ signal at the plasma membrane in RBP2 positive cells. Scale bar
382 = 1 µm.

383

384 **Larger synthetic ribbon-type AZs establish larger $Ca_V1.3$ Ca^{2+} channel clusters.**

385 Next, we tetra-transfected HEK293 cells with palm-Bassoon, Halo-tagged $Ca_V1.3\alpha_1$, RBP2 and RIBEYE
386 to explore the impact of co-expressing of RIBEYE on the clustering of $Ca_V1.3$ Ca^{2+} channels (Fig. 6A for
387 transfection scheme). Using confocal imaging of immunofluorescently labelled RIBEYE, Halo-$Ca_V1.3$
388 and Bassoon (RBP2 immunofluorescence was imaged using epifluorescence to select tetra-transfected
389 HEK293 cells), we observed colocalization of $Ca_V1.3\alpha1$, Bassoon and RIBEYE (Fig. 6B). Line profiles
390 drawn tangentially along the plasma membrane showed that beyond the general distribution of a
391 $Ca_V1.3\alpha_1$ signal in the plasma membrane, $Ca_V1.3\alpha_1$ signal hotspots occurred underneath the *SyRibbons*
392 (Fig. 6C). The signal intensity of RIBEYE immunofluorescence positively correlated with the $Ca_V1.3$
393 signal immunofluorescence, (P_r = 0.839 and 0.886 from two sample line scans, ****P < 0.0001), which
394 has previously been reported for immunolabeled native ribbon-type AZs of mouse IHCs (Ohn *et al*,
395 2016). We further performed a pixel-based correlation analysis (Supplementary Fig. 7A, B) which
396 indicated a moderate to strong colocalisation of RIBEYE and $Ca_V1.3$ upon co-expression of palm-
397 Bassoon and RBP2. In contrast, a poor colocalization was found in cells expressing only RIBEYE and
398 $Ca_V1.3$; average Pearson's colocalisation coefficient = 0.41 versus 0.24; average Mander's overlap
399 coefficient = 0.63 versus 0.34, N = 12 and 8 cells respectively (**P < 0.01m Wilcoxon's Rank Test).
400 Colocalisation quantifications for other transfection combinations shown in Fig. 2, 5 and
401 Supplementary Fig. 4 have been collectively depicted in Supplementary Fig. 7. We next turned to 2-
402 color STED imaging which provided improved spatial resolution and highlighted the confined
403 localization of $Ca_V1.3$ Ca^{2+} -channel clusters underneath *SyRibbons* as shown in Fig. 6D.

404

405

406 We performed surface renderings of confocally imaged Halo-tagged $Ca_V1.3\alpha_1$, RIBEYE and palm-
407 Bassoon immunofluorescence spots as described above for estimating the volume of *SyRibbons* and
408 the $Ca_V1.3$ Ca^{2+} channel clusters (Fig. 6E, F). This revealed significantly larger $Ca_V1.3$ Ca^{2+} channel
409 clusters when colocalizing with *SyRibbons* in HEK293 + Halo-$Ca_V1.3$ + RBP2 + *SyRibbons* cells (average
410 volume ± SD = 0.18 ± 0.28 μm^3, n_{spots}= 634, N = 13 cells, data representative of 5 transfections)
411 compared to ribbonless (i.e. non-colocalized) $Ca_V1.3$ Ca^{2+} channel clusters from the same cells (volume
412 = 0.06 ± 0.10 μm^3, n_{spots}= 1354, N = 13 cells; ****P < 0.0001, Kruskal-Wallis test with *post hoc* Dunn's
413 multiple comparison test) and $Ca_V1.3$ Ca^{2+} clusters in HEK293 cells solely expressing Halo-$Ca_V1.3$ Ca^{2+}
414 channels (volume = 0.07 ± 0.09μm^3, n_{spots}= 1281, N = 16 cells, data representative of 4 transfections;
415 ****P < 0.0001, Kruskal-Wallis test with *post hoc* Dunn's multiple comparison test). Ribbonless $Ca_V1.3$
416 Ca^{2+} channel clusters did not differ significantly regardless if co-expressing RIBEYE (P = 0.099, Kruskal-
417 Wallis test with *post hoc* Dunn's multiple comparison test, see Fig. 6F). Moreover, volumes of $Ca_V1.3$
418 cluster surfaces show a moderate positive correlation with volumes of corresponding RIBEYE surfaces
419 (P_r = 0.385, ****P < 0.0001), similar to previous observations at IHC ribbon synapses (Frank *et al*, 2009;
420 Michanski *et al*, 2023; Ohn *et al*, 2016).

421

422

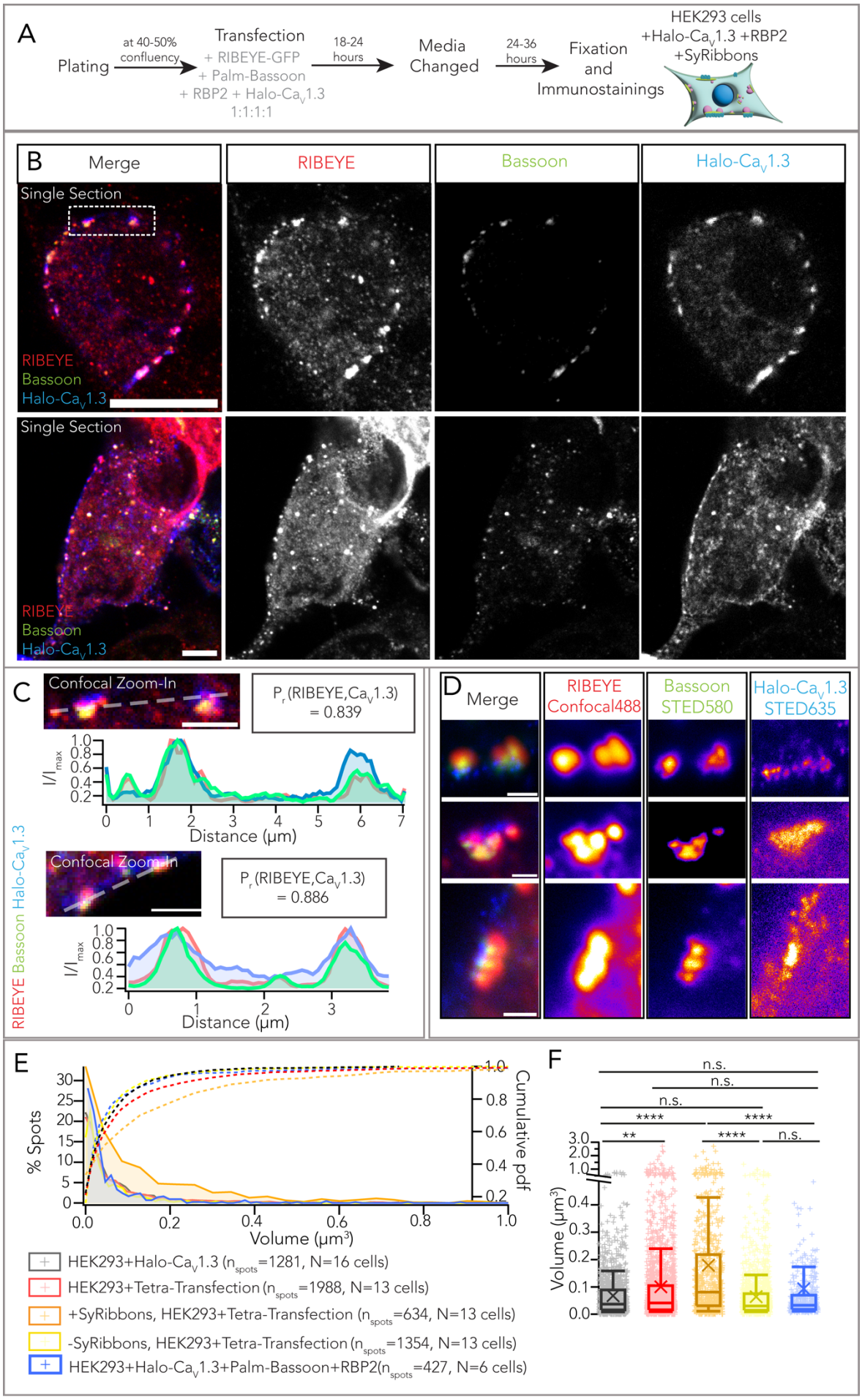
A
Plating
at 40-50% confluency
Transfection
+ RIBEYE-GFP
+ Palm-Bassoon
+ RBP2 + Halo-CaV1.3
1:1:1:1
18-24 hours
Media Changed
24-36 hours
Fixation and Immunostainings
HEK293 cells
+Halo-CaV1.3 +RBP2
+SyRibbons
B
Merge
RIBEYE
Bassoon
Halo-CaV1.3
Single Section
RIBEYE
Bassoon
Halo-CaV1.3
Single Section
RIBEYE
Bassoon
Halo-CaV1.3
C
Confocal Zoom-In
Pr(RIBEYE,CaV1.3) = 0.839
I/Imax
Distance (µm)
Confocal Zoom-In
Pr(RIBEYE,CaV1.3) = 0.886
I/Imax
Distance (µm)
RIBEYE Bassoon Halo-CaV1.3
D
Merge
RIBEYE Confocal488
Bassoon STED580
Halo-CaV1.3 STED635
E
% Spots
Cumulative pdf
Volume (µm³)
HEK293+Halo-CaV1.3 (nspots=1281, N=16 cells)
HEK293+Tetra-Transfection (nspots=1988, N=13 cells)
+SyRibbons, HEK293+Tetra-Transfection (nspots=634, N=13 cells)
-SyRibbons, HEK293+Tetra-Transfection (nspots=1354, N=13 cells)
HEK293+Halo-CaV1.3+Palm-Bassoon+RBP2(nspots=427, N=6 cells)
F
n.s.
n.s.
n.s.
****
****
**
****
n.s.
Volume (µm³)

423

424 **Figure 6 - Synthetic ribbon-type active zones recruit $Ca_V1.3$ Ca^{2+} channels.**

425 **A** Experimental scheme for expression of Halo tagged $Ca_V1.3$, palm-Bassoon, RIBEYE-GFP and RBP2
426 in HEK293 cells.

427 **B** Representative confocal images (single sections) of HEK293 cells transfected with RBP2 (not
428 shown, expression confirmed using epifluorescence), RIBEYE-GFP (red), palm-Bassoon (green),
429 Halo-$Ca_V1.3$ (blue) shows colocalization of the three latter proteins at the plasma membrane. Scale
430 bar = 5 µm.

431 **C** Confocal zoom-ins from **(B)**. Line scans depict an increased $Ca_V1.3$ signal intensity (blue) at sites
432 where RIBEYE (red) and palm-Bassoon (green) clusters localize. Pearson's correlation coefficients
433 (*Pr*) were calculated along the line profiles for RIBEYE and $Ca_V1.3$ signal intensity and indicate a
434 high degree of correlation (~0.8) between the spatial localization of the two. Scale bar = 2 µm.

435 **D** Super-resolution STED images showing $Ca_V1.3$ clusters localizing at the base of the *SyRibbons*.
436 Scale bar = 500nm.

437 **E** Distribution of volumes from confocal images of $Ca_V1.3$ clusters colocalizing with *SyRibbons*
438 (orange, n_{spots} = 634) and not colocalizing with *SyRibbons* (yellow, n_{spots} = 1354) from HEK293 cells
439 expressing $Ca_V1.3$, RBP2 and *SyRibbons* (N = 13 cells). Pooled volumes of all $Ca_V1.3$ clusters (with
440 and without *SyRibbons*) from these cells have been shown in red (n_{spots} = 1988). Volumes of $Ca_V1.3$
441 clusters from HEK293 cells expressing only Halo-$Ca_V1.3$ (black, n_{spots} = 1281, N = 16 cells) and from
442 cells expressing Halo-$Ca_V1.3$, RBP2 and palm-Bassoon (blue, n_{spots} = 427, N = 6 cells) have been
443 plotted for comparison.

444 **F** Box plot depicting data from (E). $Ca_V1.3$ clusters appear larger on an average in cells expressing
445 $Ca_V1.3$, RBP2 and *SyRibbons versus* in cells expressing only $Ca_V1.3$, (***P* = 0.0044). Within cells
446 expressing all four proteins, $Ca_V1.3$ clusters are much larger when colocalizing with *SyRibbons*
447 versus when they do not (*****P < 0.0001*). $Ca_V1.3$ clusters colocalising with *SyRibbons* were in fact
448 also larger than clusters in cells expressing only $Ca_V1.3$ and cells expressing only RBP2 and palm-
449 Bassoon (*****P < 0.0001*). Statistical test: Kruskal-Wallis test with *post hoc* Dunn's multiple
450 comparison correction. Overlaid plus signs represent individual spots, crosses represent mean
451 values, central band indicates the median, whiskers represent 90/10 percentiles and boxes
452 represent 75/25 percentiles.

453

454 **Ca^{2+} imaging reveals a partial spatial confinement of Ca^{2+} signal at synthetic ribbon-type active**
455 **zones.**

456 Finally, we set-out to functionally characterize synthetic ribbon-type AZs. We combined patch-clamp
457 recordings of $Ca_V1.3$ Ca^{2+} influx with spinning-disk confocal microscopy to visualize Ca^{2+} signals at the
458 synthetic ribbon-type AZs in HEK293 cells. Following tetracycline-induction for $Ca_V1.3$ expression,
459 HEK293 cells were co-transfected with constructs expressing RIBEYE-GFP, untagged palm-Bassoon and
460 RBP2-p2A-mKATE2, (Fig. 7A). We recorded mKATE2 positive cells that expressed peripheral GFP
461 puncta, indicative of RIBEYE and palm-Bassoon co-expression. We employed peripheral GFP
462 expression as a proxy of *SyRibbons* for functional analysis (Fig. 7B). Ruptured patch-clamp recordings
463 were performed with 10 mM $[Ca^{2+}]_e$ and 10 mM intracellular EGTA to enhance the signal to background
464 ratio for visualizing Ca^{2+} influx using the low-affinity red-shifted Ca^{2+} indicator Calbryte590 (100 µM, k_d
465 = 1.4 µM). After loading the cell for approximately a minute, we first applied step depolarizations of

466 20 ms from -83 to +62 mV in 5-mV step increments to measure Ca^{2+} current (density)–voltage relations.
467 We did not observe any changes in either the Ca^{2+} current density (*P* = 0.293, t-test) or the voltage-
468 dependence of Ca^{2+} current (*P* = 0.780, t-test when comparing V_{half}) when comparing cells expressing
469 $Ca_V1.3$ + RBP2 + *SyRibbons* with cells expressing only $Ca_V1.3$ (Fig. 7C and 7D). Next, we applied a
470 depolarizing pulse to +2 mV for 500 ms and acquired images at a frame rate of 20 Hz (Fig. 7E). The
471 intracellular Ca^{2+} signals mediated by $Ca_V1.3$ Ca^{2+} influx were visualized as an increase in Calbryte590
472 fluorescence. The increase of Calbryte590 fluorescence appeared to spread throughout the HEK293
473 cell membrane with discrete regions of higher signal intensity at *SyRibbons* (exemplary cell shown in
474 Fig. 7F with zoom-in at site with *SyRibbon* shown in 7G). We note that we did not find noticeable red
475 fluorescence at *SyRibbons* in the absence of depolarization, which is similar to findings with Fluo-4FF
476 in IHCs (Frank *et al*, 2009), but different from the situation for the large spherical presynaptic bodies
477 in bullfrog hair cells that are stained by Fluo-3 (Issa & Hudspeth, 1996). Line profiles drawn tangentially
478 to the membrane in composite ΔF image of Calbryte590 signal and RIBEYE-GFP showed a high
479 correlation between the localization of *SyRibbons* and peak intensity of Calbryte590 fluorescence
480 increase, indicating preferential Ca^{2+} signaling at the *SyRibbons* (two representative line scans shown
481 in Fig. 7H, Pearson correlation coefficients of 0.783 and 0.757). Recordings were made from 24 cells (7
482 transfections) and ROIs (diameter = 2 µm) with and without *SyRibbons* were analyzed as shown in Fig.
483 7I. Calbryte590 $\Delta F_{max}/F_0$ values were calculated for each ROI which on an average showed higher
484 $\Delta F_{max}/F_0$ values for ROIs with *SyRibbons* (on average ~26% higher) than for ROIs without *SyRibbons* (**P*
485 = 0.018, paired t-test, Fig. 7J). We note that occasionally in some cells we observed a higher
486 Calbryte590 signal increase at sites without *SyRibbons*, and we attribute this to the likely presence of
487 AZ-like clusters composed of RBP2 and palm-Bassoon in these regions which we could not visualize.

488

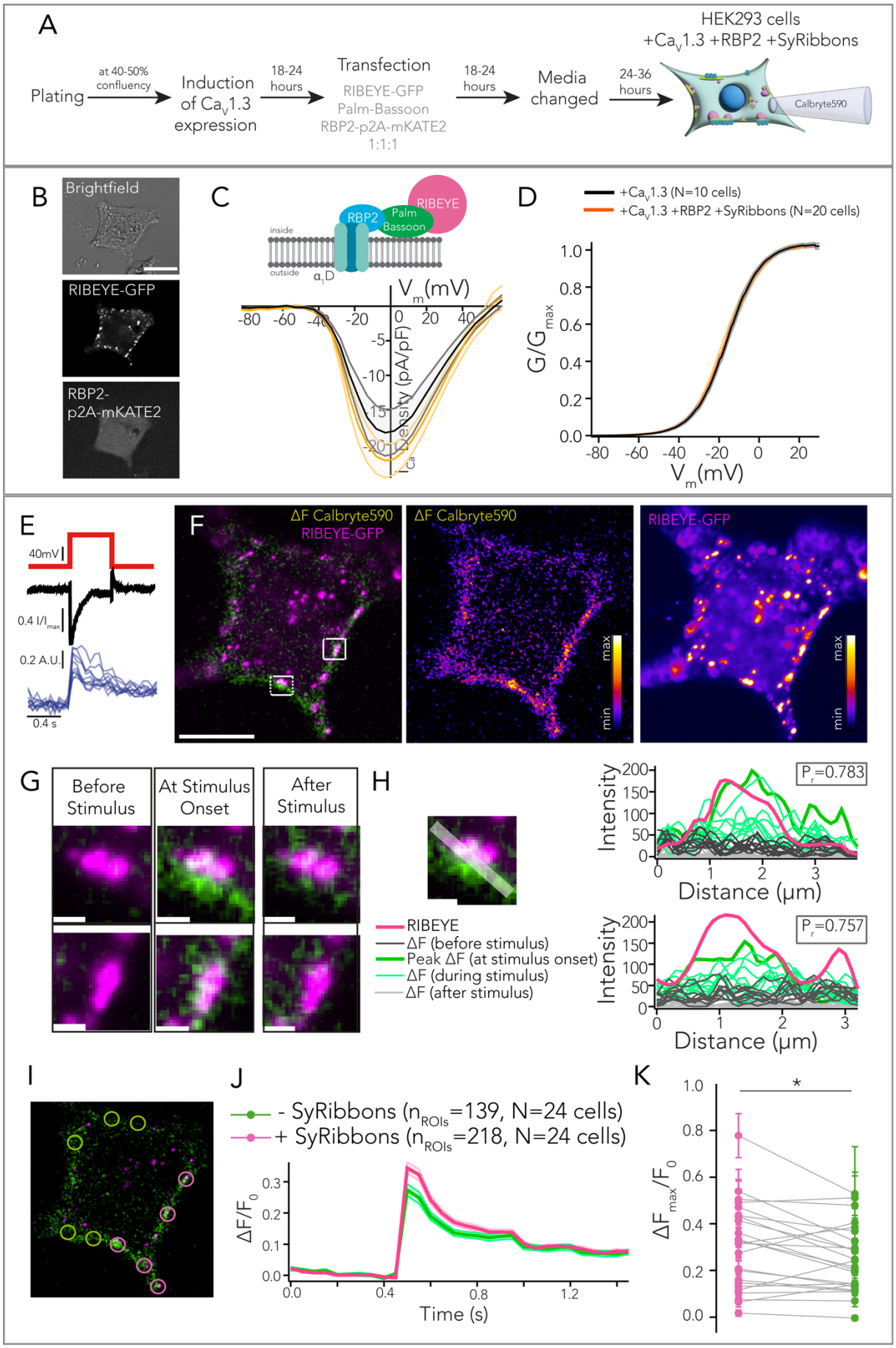
A
Plating
at 40-50% confluency
Induction of Cav1.3 expression
18-24 hours
Transfection
RIBEYE-GFP
Palm-Bassoon
RBP2-p2A-mKATE2
1:1:1
18-24 hours
Media changed
24-36 hours
HEK293 cells
+Cav1.3 +RBP2 +SyRibbons
Calbryte590
B
Brightfield
RIBEYE-GFP
RBP2-p2A-mKATE2
C
RIBEYE
RBP2
Palm Bassoon
inside
outside
α1D
Vm(mV)
Density (pA/pF)
D
+Cav1.3 (N=10 cells)
+Cav1.3 +RBP2 +SyRibbons (N=20 cells)
G/Gmax
Vm(mV)
E
40mV
0.4 I/Imax
0.2 A.U.
0.4 s
F
ΔF Calbryte590
RIBEYE-GFP
ΔF Calbryte590
RIBEYE-GFP
max
min
G
Before Stimulus
At Stimulus Onset
After Stimulus
H
RIBEYE
ΔF (before stimulus)
Peak ΔF (at stimulus onset)
ΔF (during stimulus)
ΔF (after stimulus)
Intensity
Distance (µm)
Pr=0.783
Pr=0.757
I
J
- SyRibbons (nROIs=139, N=24 cells)
+ SyRibbons (nROIs=218, N=24 cells)
ΔF/F0
Time (s)
K
ΔFmax/F0
*

489

490

491 **Figure 7 - Ca^{2+} imaging reveals higher Ca^{2+} signal intensity underneath *SyRibbons.***

492 **A** Experimental scheme for expression of *SyRibbons*, RBP2 and $Ca_V1.3$ in HEK293 cells for patch
493 clamp in combination with Ca^{2+} imaging using the low affinity Ca^{2+} indicator Calbryte590.

494 **B** Exemplary cell used for Ca^{2+} imaging. Cells were identified by peripheral RIBEYE-GFP puncta
495 as shown (indicative of RIBEYE and palm-Bassoon co-expression) and mKATE2 signal
496 (indicative of RBP2 expression).

497 **C** Current density-voltage (IV) relations from whole-cell patch clamp recordings of HEK293 cells
498 expressing $Ca_V1.3$ + RBP2 + *SyRibbons* (n=20, in orange) and only $Ca_V1.3$ (n=10, in black). Lines
499 represent mean current traces, shaded area represents ± SEM. Whole-cell Ca^{2+} current density
500 does not appear to change upon co-expression of RBP2 and *SyRibbons* (P = 0.293, t-test).

501 **D** The voltage-dependence of Ca^{2+} current influx does not seem to be altered upon co-
502 expression of RBP2 and *SyRibbons* at the whole-cell level.

503 **E** A depolarizing pulse to +2mV was applied to the cells for 500 ms and the increase in
504 Calbryte590 fluorescence was measured by acquiring images at a frame rate of 20 Hz using a
505 spinning disk confocal microscope.

506 **F** Representative image of a HEK293 cell expressing *SyRibbons*, RBP2 and $Ca_V1.3$ stimulated as
507 described in (E). RIBEYE-GFP signal has been shown in magenta; the change in Calbryte590
508 fluorescence intensity (ΔF) upon Ca^{2+} binding (the frame at the onset of depolarization to
509 +2mV) has been shown in green. Note the distinct Ca^{2+} signal "hotspots" that co-localize with
510 *SyRibbons*. Scale bar = 10 µm.

511 **G** Zoom-ins from (F). Frames before, at the onset of, and after stimulation have been shown.
512 Note the localized Ca^{2+} influx at the base of the *SyRibbons*. Scale bar = 1 µm.

513 **H** Line profiles drawn tangentially to the membrane in composite ΔF image of Calbryte590 signal
514 and RIBEYE-GFP show a high correlation between the localization of *SyRibbons* and peak
515 intensity of Calbryte590 fluorescence increase (P_r = ~0.7). Plots show intensity profiles along
516 line scans for RIBEYE-GFP (magenta) and Calbryte590 (light grey for frames before stimulus,
517 bold green for peak intensity at onset of stimulus, light green lines for decaying intensity
518 during ongoing stimulus and dark grey for frames post-stimulus).

519 **I** Regions of interest (ROIs) of 2 µm diameter were drawn at sites with (magenta circles) and
520 without (green circles) *SyRibbons* and the corresponding Calbryte590 $\Delta F/F_0$ values were
521 calculated for each ROI.

522 **J** Plot of average (shaded area represents ± SEM) $\Delta F/F_0$ values from ROIs with and without
523 *SyRibbons* (218 and 139 ROIs respectively from N = 24 cells, data from 7 transfections).

524 **K** On average, Calbryte590 $\Delta F_{max}/F_0$ was higher for ROIs with *SyRibbons* than ROIs without them
525 in a given cell (*P = 0.018, paired t-test). Dots represent mean of $\Delta F_{max}/F_0$ from ROIs with
526 (magenta) and without (green) *SyRibbons* averaged per cell, error bars represent ± SEM.

527

528

529 ## Discussion

530 In this study, we reconstituted and characterized a minimal ribbon-type AZ model system using
531 heterologous expression. Co-expressing $Ca_V1.3$ Ca^{2+} channels with membrane targeted Bassoon for
532 RIBEYE anchorage to the plasma membrane and attracting exogenous RBP2 for clustering Ca^{2+}
533 channels in HEK293 cells led to structures recapitulating basic aspects of IHC ribbon synapses. Despite
534 the poor regulation of transgene expression in the synapse-naïve HEK293 cells, the AZ-like structures,
535 in the subset of cells were similar in morphology to the native IHC AZs. This applied to the *synthetic*
536 ribbons as well as to the AZ-like clusters of Bassoon, RBP2 and $Ca_V1.3$ Ca^{2+} channels. However, all three
537 components exhibited variability beyond the substantial natural heterogeneity found among the IHC
538 AZs (Moser *et al*, 2023). Although expression of RIBEYE does not seem to affect $Ca_V1.3$ physiology and
539 kinetics, we demonstrate enhanced clustering of $Ca_V1.3$ channels and localization of Ca^{2+} influx at
540 *SyRibbons*, with a mild increase in Ca^{2+} signal intensity. As *SyRibbons* partially resemble native hair cell
541 AZs, we expect this easily available and experimentally accessible system to serve as an advanced
542 testbed for functional interactions of AZ proteins and Ca^{2+} channels. Further efforts towards
543 reconstituting SVs and their release sites will help to enhance the utility of these synthetic AZs.
544

545 ### Synthetic active zone reconstitution model to study ribbon synapse assembly

546 By demonstrating that membrane-targeted Bassoon suffices to anchor ribbon-like RIBEYE assemblies,
547 this work adds to the top-down and bottom-up evidence for a key role of Bassoon in attracting RIBEYE
548 to the presynaptic density at the AZ in photoreceptors and hair cells (Dick *et al*, 2003; Khimich *et al*,
549 2005; Jing *et al*, 2013; tom Dieck *et al*, 2005). Additional expression of multi-domain proteins of the
550 presynaptic density such as CAST (Ohtsuka *et al*, 2002; Inoue *et al*, 2006) might avoid the need for
551 artificial palmitoylation of Bassoon for membrane targeting. Furthermore, our results support a model
552 of a bidirectional control of AZ size and shape by RIBEYE and proteins of the presynaptic density. The
553 amount of RIBEYE assembled in membrane localized *SyRibbons* appeared regulated strongly
554 contrasting the seemingly unregulated cytosolic RIBEYE assemblies dominating HEK293 cells in the
555 absence of membrane-targeted Bassoon. Vice versa, clusters of Bassoon at the plasma membrane
556 were larger at *SyRibbons* than in the absence of RIBEYE. Finally, the size of *SyRibbons* seemingly scaled
557 with the size of $Ca_V1.3$ and Bassoon clusters similar to what is observed in IHCs (Ohn *et al*, 2016). Such
558 a model is consistent with results from genetic perturbation of native ribbon synapses: i) disruption of
559 RIBEYE leads to a disintegration of Bassoon into smaller subclusters in IHCs (Jean *et al*, 2018), and ii)
560 disruption of CAST and ELKS reduces the size of the ribbon-type AZs in rod photoreceptors (tom Dieck
561 *et al*, 2012; Hagiwara *et al*, 2018). We speculate that achieving the full extent of large ribbon-type AZs
562 such as in rod photoreceptors as well as regulating the size of ribbon-type AZs at a specific synapse
563 according to the precise functional demands requires such a functional interplay between proteins of

564 the presynaptic density and RIBEYE. We note that other ribbon-resident proteins such as piccolino
565 likely contribute to this fine-tuning of the size and shape of ribbon-type AZs, which will be an exciting
566 question for future studies. Indeed, disruption of piccolino in IHCs reduced the average ribbon size
567 (Müller *et al*, 2019; Michanski *et al*, 2023). One exciting example of ribbon synapse heterogeneity
568 manifests itself in IHCs where synapses show a spatial size gradient that likely relates to the diverse
569 molecular and functional properties of the postsynaptic SGNs (reviewed in Moser *et al*, 2023).

570 **Insights into presynaptic Ca^{2+} channel clustering and function**

571 Current discussion of the clustering of Ca_V Ca^{2+} channels offers two different models: low affinity
572 protein-protein interactions (e.g. Hibino *et al*, 2002; Kaeser *et al*, 2011) via specific domains and liquid-
573 liquid phase separation involving intrinsically disordered domains (e.g. Heck *et al*, 2019). Work on
574 ribbon synapses has considered layers of organizing Ca_V Ca^{2+} channels at the AZ that seem more
575 compatible with the former model: i) "micro-clustering" to which the synaptic ribbon contributes as a
576 super-scaffold (Jean *et al*, 2018; Neef *et al*, 2018; Frank *et al*, 2010; Maxeiner *et al*, 2016) and ii)
577 tethering and "nano-clustering" by RBPs, RIMs, CAST and ELKS (Liu *et al*, 2011; Grabner *et al*, 2015;
578 Jung *et al*, 2015; Krinner *et al*, 2017; Luo *et al*, 2017; Hagiwara *et al*, 2018). Moreover, there is
579 converging evidence for nanoscale coupling of few Ca_V Ca^{2+} channels to SV release sites (Brandt, 2005;
580 Jarsky *et al*, 2010; Wong *et al*, 2014; Maxeiner *et al*, 2016; Özçete & Moser, 2021; Grabner & Moser,
581 2021; Jaime Tobón & Moser, 2023) for which a role of the ribbon has been more controversial (e.g.
582 Maxeiner *et al*, 2016; Grabner & Moser, 2021). MINFLUX nanoscopy of rod photoreceptor AZs recently
583 revealed a well-ordered double-line array topography of Ca_V Ca^{2+} channels, RIM, Bassoon and
584 ubMunc13-2 at the presynaptic membrane on both sides of the ribbon (Grabner *et al*, 2022).

585 Clearly, we could not fully reconstitute this complex organization with the minimal set of molecular
586 players at *SyRibbons* in HEK293 cells. Yet, we demonstrate a positive effect of *SyRibbons* on local Ca^{2+}
587 signaling, recapitulating microclustering of $Ca_V1.3$ Ca^{2+} channels at IHC ribbon synapses. However, we
588 note that the functional impact of ribbon-mediated clustering of $Ca_V1.3$ Ca^{2+} channels remains unclear
589 at the moment. Our Ca^{2+} imaging data seems more reminiscent of previous work on ribbon-type AZs
590 of immature IHCs (Wong *et al*, 2014) where a broader distribution of $Ca_V1.3$ and ribbons go along with
591 an immature state of the IHC AZs. We also note that the difference in Ca^{2+} signalling near or apart
592 *SyRibbons* is rather subtle. We propose two explanations in this regard: (i) the use of an overexpression
593 system diminishes the contrast of the Ca^{2+} signal between AZ-like domains and the regular membrane.
594 Overexpressed $Ca_V1.3$ is likely distributed diffusely across the plasma membrane in these cells along
595 with more localised $Ca_V1.3$ clusters observed at *SyRibbons* (see Fig. 6B lower panel). (ii) While the
596 presence of *SyRibbons* appears to promote the formation of larger $Ca_V1.3$ channels and partially
597 localise the Ca^{2+} signal, it is unlikely that *SyRibbons* recruit a larger Ca^{2+} channel complement. IHCs of

598 RIBEYE KO mice were reported to show normal Ca^{2+} current amplitudes at the whole-cell and single-
599 AZ level (Jean *et al*, 2018), while the spatial spread of the Ca^{2+} signal was more diffuse in the absence
600 of the ribbon.

601 We propose that *SyRibbons* scaffold $Ca_V1.3$ channel nano-clusters in a non-native heterologous
602 expression system resulting in an increased channel density in regions with *SyRibbons*. In support of
603 this hypothesis, the Ca^{2+} signal averaged at *SyRibbons* showed a mildly increased maximal amplitude
604 when compared with diffuse Ca^{2+} channel distribution in the absence of *SyRibbons.* Instead, the total
605 number of channels may be unaffected, which would explain why Ca^{2+} current amplitudes at the
606 whole-cell level are not impacted by expression of *SyRibbons*. A clear limitation in the study therefore
607 arises from the use of an overexpression system, making it necessary to interpret results with caution
608 and requiring *in vivo* and *ex vivo* validation. Future use of polycistronic gene expression or stable cell
609 lines expressing all components could help with more consistent expression of the components and
610 make the system become even more widely applicable.

611 Another limitation of the synthetic AZ system in HEK293 cells is the lack of SVs and the molecular
612 machinery required for SV release. Nonetheless, our work paves the way for future studies including
613 stable co-expression of AZ proteins including of the release site marker Munc13-1 (Sakamoto *et al*,
614 2018; Böhme *et al*, 2016) and potential delivery of SV machinery via co-expression (Park *et al*, 2021).
615 Alternatively, using neurosecretory cells such as pheochromocytoma cells (PC12) or adrenal
616 chromaffin cells in primary culture, offer the advantage of providing synaptic-like microvesicles and a
617 large set of components of the presynaptic machinery such that expression of exogenous proteins
618 might be limited to RIBEYE. On the other hand, the complex molecular background involving various
619 types of Ca_V channels will likely complicate the interpretation. Regardless, *SyRibbons* in cultured cells
620 offer great availability and as adherent cells, are well accessible to sophisticated analysis by techniques
621 such MINFLUX nanoscopy and cryo-electron tomography.

622

623 Materials and Methods

624 HEK cell culture and transfections

625 In this study, we used human embryonic kidney (HEK293) cells stably expressing a tetracycline-
626 inducible human $Ca_V1.3$ pore forming α_1-D subunit transgene (CACNA1D, NM_000720.2), and showing
627 constitutive expression of $Ca_V\beta_3$ (CACNB3, NM_000725.2) and $Ca_V\alpha_2\delta$-1 (CACNA2D1, NM_000722.2).
628 The stably expressing cell line was acquired from Charles River Laboratories, Cleveland, Ohio, USA (Cat.
629 No. CT6232). The cells were cultured as per product protocols in Dulbecco's Modified Eagle Medium
630 (DMEM) containing GlutaMax, high glucose and pyruvate (Gibco, Life Tech., 31966047), supplemented
631 with 10% Fetal Bovine Serum (FBS; Gibco, Life Tech., A5256701) and 100 units/ml of Penicillin-

632 Streptomycin (Gibco, Life Tech., 15070063). Additionally, the media was supplemented with 0.6 µM of
633 Isradipine (Sigma Aldrich, I6658) and the following selection antibiotics (in mg/ml): 0.005 Blasticidin
634 (Invivogen, ant-bl-05), 0.50 Geneticin (G418 Sulfate; Gibco, Life Tech., 10131027), 0.10 Zeocin
635 (InvivoGen, ant-zn-05) and 0.04 Hygromycin (Thermo Fisher, 10687010). Cells were cultured in a
636 humidified incubator at 37˚C with 5% (v/v) CO_2 saturation. Cells were split at ~70% confluency every
637 3-4 days to prevent adverse effects on cell growth and channel expression, by dissociating the cell
638 using Accutase (Sigma-Aldrich, A6964). The passage number did not exceed more than 26 passages.
639 For experiments, cells were grown in media lacking selection antibiotics. For induction of α_1-D subunit
640 expression, cells were treated with selection antibiotic-free medium containing 3 µg/ml tetracycline.
641 For transfection, 6.8 µg polyethylenimine (PEI, 25kDa linear, Polysciences, 23966) was added along
642 with a total of 2 µg of DNA to a final volume of 100 µl of DMEM (without FBS). The PEI/DNA mixture
643 was thoroughly mixed and allowed to incubate for 30 min at room temperature before being added to
644 the cells (30 µl/well in a 24-well-plate containing 500 µl media, cell confluency ~50-70%). For all
645 experiments with co-transfections, we used an equimolar ratio of DNA (total amount of DNA was kept
646 2 µg in a 100 µl transfection mix). After 18-24 hours, transfection media was replaced with fresh media
647 devoid of selection antibiotics. Cells were used for experiments (immunocytochemistry, patch clamp
648 and Ca^{2+} imaging) 24-48 hours after changing the media or as specified. If cell confluency was too high,
649 cells were reseeded to an appropriate confluency and allowed to settle for at least 12 hours before
650 commencement of experiments.
651
652 **Expression vectors for RIBEYE, Bassoon, $Ca_V1.3$ and RBP2**
653 **Table 1: List of plasmids**

Plasmid Name	Backbone	Promoter	Insert	Antibiotic Resistance	Regulatory Elements	Reference
RIBEYE-GFP	pAAV-GFP	CMV-HBA	human RIBEYE-GFP	Ampicillin	WPRE	
Bassoon	pCS2+	CMV	Rat Bassoon	Kanamycin	SV40 poly(A)	
Palm-Bassoon-GFP	pEGFP-C1	CMV enhancer	Palm-rat Bassoon (95-3938)-EGFP	Kanamycin	SV40 poly(A)	
Palm-Bassoon-STOP	pEGFP-C1	CMV enhancer	Palm-rat Bassoon (95-3938)-STOP	Kanamycin	SV40 poly(A)	

EGFP-$Ca_V1.3$	pHTN	CMV enhancer-promoter	EGFP-human *CACNA1D*	Ampicillin	SV40 poly(A)	(Schwenzer *et al*, 2024)
Halo-$Ca_V1.3$	pHTN	CMV enhancer-promoter	HaloTag-human *CACNA1D*	Ampicillin	SV40 poly(A)	
RBP2-p2A-mKATE2	f(syn)w	CMV enhancer	mKATE2-p2A-RBP2	Ampicillin	WPRE, SV40 poly(A)	
RBP2	pAAV	CMV enhancer-HBA	RBP2	Ampicillin	WPRE, SV40 poly(A)	

654

655 The RIBEYE-GFP construct used consisted of a human RIBEYE cDNA cloned inframe into a pAAV-GFP
656 vector driven by a hybrid CMV-enhancer-human-beta-actin promoter (CMV-HBA) and containing a
657 downstream Woodchuck Hepatitis Virus (WHV) Posttranscriptional Regulatory Element (WPRE) for
658 mRNA stabilization. All Bassoon constructs encode rat Bassoon. The untagged full-length constructs
659 were cloned in the pCS2+ vector. For the generation of palm-Bassoon constructs, we used a pEGFP-C1
660 vector backbone with a CMV promoter and kanamycin resistance cassette. The insert comprised of a
661 palmitoylation consensus sequence of GAP43
662 (ATGCTGTGCTGTATGAGAAGAACCAAACAGGTTGAAAAGAATGATGAGGACCAAAAGATTTCCGGACTCAGA
663 TCTCGAG), followed by a cDNA sequence encoding amino acids 95-3938 of rat Bassoon, and a C-
664 terminal monomeric GFP. For the untagged version, the GFP tag was replaced by a STOP codon. To
665 generate the Halo-$Ca_V1.3$ plasmid (Schwenzer *et al*, 2024), human $Ca_V1.3$ cDNA (accession number
666 NM_001128840.2) was de-novo synthesized and assembled into a HaloTag vector (Promega G7721)
667 using restriction cloning, thus encoding an N-terminal fusion of $Ca_V1.3$ to HaloTag linked by a 'GGS'
668 sequence. The analogous GFP-$Ca_V1.3$ plasmid was generated by exchanging the HaloTag sequence for
669 mEGFP using restriction cloning. The RBP2 construct with an mKATE2 tag comprised of an insert coding
670 for mouse RBP2 (accession ID NP_001074857.1) with a p2A cleavage site followed by a C-terminal
671 mKATE2 cloned inframe into a f(syn)w-mKATE2-p2A vector driven by a CMV promoter-enhancer and
672 containing downstream WPRE sequence. The untagged version was made by cloning the RBP2 cDNA
673 from this plasmid and replacing RIBEYE-GFP in the pAAV-CMV-HBA-RIBEYE-GFP-WPRE plasmid by in-
674 fusion cloning (Takara Bio USA, Inc.).

675

676 **Immunocytochemistry and Imaging**

677 HEK293 cells plated on poly-L-lysine coated coverslips were fixed with 99% chilled methanol at -20˚C
678 for 2 minutes as previously described (Picher *et al*, 2017b). The coverslips were washed thoroughly
679 three times with PBS at room temperature (5 – 10 min). Blocking and permeabilization was performed
680 with GSDB (goat serum dilution buffer: 16% normal goat serum, 450 mM NaCl, 0.3% Triton X-100,

681 20mM phosphate buffer, pH ~7.4) for 45-60 minutes at room temperature. Samples were incubated
682 with respective primary antibodies (diluted in GSDB, refer to Table 2) overnight at 4˚C or for 2 hours
683 at RT. The samples were then washed three times (5–10 minutes each) with wash buffer (450 mM
684 NaCl, 0.3% Triton X-100, 20mM phosphate buffer, pH ~ 7.4). Incubation with appropriate secondary
685 antibodies (also diluted in GSDB refer to Table 2) was performed for 1 hour at room temperature in a
686 light-protected wet chamber. Lastly, the coverslips were washed three times with wash buffer (5-10
687 minutes each) and one final time with PBS, before mounting onto glass slides with a drop of
688 fluorescence mounting medium (Mowiol 4-88, Carl Roth). For live cell imaging of cells transfected with
689 Halo-Ca_V1.3 (Fig. 4B, C), cells plated on glass-bottomed dishes were treated with Janelia Fluor 646
690 HaloTag Ligand (Promega, Cat. No. GA1120) at a final labelling concentration of 200nM (in cell culture
691 media). Cells were incubated with the ligand for ~60 min at 37˚C with 5% (v/v) CO_2 saturation, after
692 which the media was replaced with an equal volume of fresh warm culture media.
693 Images from fixed and live samples were acquired in confocal/ STED mode using an Olympus IX83
694 inverted microscope combined with an Abberior Instruments Expert Line STED microscope (Abberior
695 Instruments GmbH). We used lasers at 488, 561, and 633 nm for excitation and a 775 nm (1.2W) laser
696 for stimulated emission depletion. 1.4 NA 100X or 20X oil immersion objectives were used for fixed
697 samples, and a water immersion 60X objective was used for live samples. Confocal stacks or single
698 sections were acquired using *Imspector* Software (pixel size = 80 X 80 nm along xy, 200 nm along z).
699 For 2D-STED images, a pixel size of 15 X 15 nm (in xy) was used. Images in Supplementary Fig. 2A were
700 acquired using a Leica SP8 confocal microscope (Leica Microsystems, Germany). All acquired images
701 were visualized using NIH ImageJ software and adjusted for brightness and contrast. Samples and their
702 corresponding controls were processed in parallel using identical staining protocols, laser excitation
703 powers and microscope settings.
704
705 **Table 2: List of antibodies**

Antibody	Host specie	Company	Dilution	Identifier
Anti-GFP	Chicken	Abcam	1:200	Ab13970
Anti-CtBP2	Mouse (monoclonal IgG1)	BD Biosciences	1:200	612044
Anti-RIBEYE-A	Guinea pig	Synaptic Systems	1:200	192104
Anti-RIBEYE-A	rabbit	Synaptic Systems	1:200	192103
Anti-RIBEYE-B	rabbit	Synaptic Systems	1:200	192003
Anti-Bassoon	chicken	Synaptic Systems	1:200	141016
Anti-Bassoon	mouse	Abcam	1:200	Ab82958
Anti-Na, K-ATPase α_1	mouse	Abcam	1:200	Ab7671
Anti-Calnexin	rabbit	Abcam	1:200	Ab22595
Anti-GM130	mouse	BD Biosciences	1:200	610822

Anti-LAMP1 (CD107A)	mouse	eBioscience	1:200	14-1079-80
Anti-Halo	mouse	Promega	1:200	G9211
Anti-RBP2	rabbit	Synaptic Systems	1:200	316103
Anti-$Ca_V1.3$	rabbit	Alomone	1:100	ACC005
Alexa Fluor 488 conjugated anti-chicken	Goat IgG (H+L)	Invitrogen	1:200	A11039
Alexa Fluor 488 conjugated anti-guinea pig	Goat IgG (H+L)	Invitrogen	1:200	A11073
Alexa Fluor 488 conjugated anti-rabbit	Goat IgG (H+L)	Invitrogen	1:200	A11008
Alexa Fluor 488 conjugated anti-mouse	Goat IgG (H+L)	Invitrogen	1:200	A11001
Alexa Fluor 405 conjugated anti-rabbit	Goat IgG (H+L)	Invitrogen	1:200	A31556
Alexa Fluor 546 conjugated anti-mouse	Goat IgG (H+L)	MoBiTec	1:200	A11003
Alexa Fluor 568 conjugated anti-chicken	Goat IgG (H+L)	Abcam	1:200	Ab175711
Alexa Fluor 568 conjugated anti-guinea pig	Goat IgG (H+L)	Invitrogen	1:200	A11075
Alexa Fluor 568 conjugated anti-rabbit	Goat IgG (H+L)	Thermo Fisher	1:200	A11011
Alexa Fluor 647 conjugated anti-mouse	Goat IgG (H+L)	Invitrogen	1:200	A21236
Alexa Fluor 647 conjugated anti-rabbit	Goat IgG (H+L)	Invitrogen	1:200	A21244

STAR Red conjugated anti-chicken	Goat IgY	Abberior	1:200	2-0102-011-2
STAR 635p conjugated anti-mouse	Goat IgG (H+L)	Abberior	1:200	ST635P-1001-500UG
STAR 635p conjugated anti-rabbit	Goat IgG (H+L)	Abberior	1:200	2-0012-007-2
STAR 580 conjugated anti-mouse	Goat IgG (H+L)	Abberior	1:200	ST580-1001-500UG

706

707 **Ultrastructural analysis using cryo-correlative electron-light microscopy**

708 HEK293 cells were transfected with RIBEYE-GFP and untagged palm-Bassoon constructs as described
709 above. The next day, the cells were detached using Accutase (Sigma-Aldrich, A6964) and replated on
710 electron microscopy grids (R2/2, Au 200 mesh, 100 holey SiO_2 film; Quantifoil) at a density of 20,000
711 cells/grid. After 24 hours, grids were vitrified by plunge-freezing in liquid ethane/propane using a
712 house-made manual plunger. Cryo-focused ion beam milling and cryo-correlative light and electron
713 microscopy were performed as previously described (Rigort *et al*, 2010; Pierson *et al*, 2024). In brief,
714 upon transferring into an Aquilos 2 focused-ion beam/scanning electron microscope (ThermoFisher
715 Scientific), the samples were imaged with an integrated fluorescent light microscope (ThermoFischer
716 Scientific) at 470 nm excitation wavelength to locate cells expressing peripheral GFP, which
717 corresponded to membrane-localised *SyRibbons*. Milling was performed at a 9° angle at these areas,
718 using ion currents between 500 nA and 100 nA. During milling, the GFP fluorescence was monitored
719 additionally when the lamellae reached 2 µm and 150 nm thickness to ensure that the structures of
720 interest were captured. All fluorescent data is shown as maximum intensity projections of 4 µm z-
721 stacks. For visualization purposes, the fluorescent image shown in Fig. 3A was corrected using the
722 rolling ball background subtraction algorithm implemented in Fiji (Schindelin *et al*, 2012; Sternberg,
723 1983). After milling, lamellae were transferred into a Krios G4 cryo-transmission electron microscope
724 (cryo-TEM; ThermoFisher Scientific). Correlation of fluorescence on 150 nm lamellae and 8700x TEM
725 overview revealed electron-dense structures at GFP puncta. Tilt series of these densities were
726 collected at 33k magnification using a dose-symmetric scheme (from -45° to +63°, 9° pretilt, 3°
727 increments) and with a 20 eV energy filter. The total electron dose was 120 $e^-/Å^2$. The data was
728 acquired using SerialEM (Mastronarde, 2005) running PACEtomo script (Eisenstein *et al*, 2023). Data
729 pre-processing and tomogram reconstruction from tilt series were done automatically using an in-
730 house script implementing MotionCor2, CTFFIND4 and IMOD
731 (https://github.com/rubenlab/snartomo; Zheng *et al*, 2017; Rohou & Grigorieff, 2015; Mastronarde,

732 1997). To enhance contrast, a Wiener-like filter was applied
733 (https://github.com/dtegunov/tom_deconv) on the tomograms.
734

735 ## Patch clamp and calcium imaging

736 $Ca_V1.3$ stably expressing HEK293 cells were plated on coverslips till about 40-50% confluency was
737 achieved, following which they were induced for $Ca_V1.3\alpha1$-D expression by incubating them for 24-48
738 hours in induction media supplemented with tetracycline. For transfected cells, transfection was
739 performed after 24hrs of induction in the induction media as explained above. Cells were recorded in
740 extracellular solution containing (in mM): 150 choline-Cl, 10 HEPES, 1 $MgCl_2$ and 10 $CaCl_2$; pH was
741 adjusted to 7.3 with CsOH and osmolality was 300-310 mOsm/kg. For electrophysiological recordings
742 in Supplementary Fig. 5 and 6, pipette solution contained (in mM): 140 NMDG, 10 NaCl, 10 HEPES, 5
743 EGTA, 3 Mg-ATP and 1 $MgCl_2$. pH was adjusted to 7.3 with methanesulfonic acid and osmolality was
744 around 290 mOsm/kg. For Ca^{2+} imaging in Fig. 7, the pipette solution contained (in mM): 111 Cs-
745 glutamate, 1 $MgCl_2$, 1 $CaCl_2$, 10 EGTA, 13 TEA-Cl, 20 HEPES, 4 Mg-ATP, 0.3 Na-GTP, 1 L-glutathione, 0.1
746 Calbryte590 (AAT Bioquest, Cat. No. 20706); pH was adjusted to 7.3, osmolality to 290 mOsm/kg.
747 Resistance of patch pipettes was 3–7 MΩ. HEK293 cells were rupture patch clamped with EPC-10
748 amplifier (HEKA electronics, Germany) controlled by *Patchmaster* software at room temperature, as
749 described previously (Picher *et al*, 2017b, 2017a). Cells were kept at a holding potential of -91.2 or -88
750 mV. All voltages were corrected for liquid junction potential offline (21.2 mV or 18 mV). Currents were
751 leak corrected using a p/10 protocol. Recordings were discarded when leak current exceeded -50 pA,
752 R_s exceeded 15 MΩ or offset potential fluctuated more than 5 mV. Current voltage (IV) relations were
753 recorded around 1 minute after rupturing the cell, by applying increasing step-depolarisation pulses of
754 voltage ranging from -86.2 mV to 58.8 mV, in steps of 5 mV. Depolarisation pulses of 500 ms were used
755 for measure $Ca_V1.3$ inactivation in Supplementary Fig. 6.

756 For Ca^{2+} imaging experiments, we used a Yokogawa CSU-X1A spinning-disk confocal scanner, mounted
757 on an upright microscope (Zeiss Examiner) with a 63X, 1.0 NA objective (W Plan-Apochromat, Zeiss).
758 Images were acquired using an Andor Zyla sCMOS 4.2 camera, controlled by *VisiView* 5.0 software
759 (Visitron Systems GmbH). GFP, mKATE2 and the low-affinity Ca^{2+} indicator Calbryte590 were excited
760 by a VS Laser Merge System (Visitron Systems) with 488 and 561 nm laser lines. Spinning disk was set
761 to 5000 rpm. mKATE2 positive cells showing peripheral GFP expression (indicative of RIBEYE and palm-
762 Bassoon co-expression) were identified and used for recordings. The cell was loaded for approximately
763 a minute with Calbryte590 dye, after which we applied step depolarizations of 20 ms from -83 to +62
764 mV in 5-mV step increments to measure Ca^{2+} current (density)–voltage relations. Next, a central plane
765 of the cell was selected and the GFP fluorescence (green channel) of the cell showing *SyRibbons* was

766 imaged. This was immediately followed by imaging of the increments of Calbryte590 fluorescence (red
767 channel) in the same plane triggered by a depolarizing pulse to +2 mV for 500 ms (frame rate = 20 Hz).
768 For Ca^{2+} imaging experiments, we also included occasionally occurring HEK293 cells which were
769 electrically coupled with other neighbouring HEK293 cells. For such cells, we could not fully
770 compensate for the slow capacitive currents and we did not use them for electrophysiological analysis.

771 **Data analysis**

772

773 **Analysis of confocal images**

774 All images were processed using NIH ImageJ software to make z-projections and multi-channel
775 composites, and figures were created using Adobe Illustrator. For analysis of membrane distribution,
776 a region of interest (ROI) of 1 µm thickness was drawn along the periphery of the cell which was
777 identified either using Na, K ATPase α_1 immunofluorescence or by enhancing the contrast in images of
778 transfected cells so that the cell boundary becomes distinguishable. Mean pixel intensity was
779 measured along this ROI and for the area enclosed within the ROI. The ratio of the mean pixel intensity
780 (periphery: inside) per cell was reported as an average from at least three central planes; we did not
781 use the basal and top plane. For volumetric fits of *SyRibbons,* IHC ribbons and Ca^{2+} channel clusters, we
782 used the inbuilt surface detection algorithm from Imaris 9.6 (Oxford Instruments). The surface detail
783 was set to 0.16 µm and largest sphere diameters for background subtraction were set as follows: for
784 RIBEYE/CtBP2 0.3 µm, for Bassoon 0.1 µm and for $Ca_V1.3$ 0.08 µm. Thresholding was performed based
785 on the quality of immunofluorescence to ensure all discernible surfaces were detected. All surfaces
786 with less than 10 voxels were filtered out. A manual check was done to include undetected surfaces,
787 remove surfaces not localizing within cell of interest, and split surfaces that would occasionally be
788 clubbed together. For analysis of *SyRibbons*, only RIBEYE surfaces colocalizing with palm-Bassoon
789 surfaces were used for quantifications (at 0.06 µm or less). Occasionally we would detect surfaces with
790 volumes larger than 2 μm^3 (usually cytosolic) or smaller than 0.02 μm^3, which were not considered for
791 analysis. For $Ca_V1.3$ cluster volumetric analysis in tetra-transfected cells, clusters classified as
792 *+SyRibbons* were at 0.045 µm or less from palm-Bassoon positive RIBEYE surfaces. All other clusters
793 were classified as *–SyRibbons*. Only clusters localized at the periphery of the cell were used for analysis.
794 Pixel-based intensity correlation analysis was performed using the *Coloc 2* plugin on ImageJ
795 (http://imagej.net/Coloc_2). Analysis was performed on 1 µm thick regions of interests marking the
796 periphery of the cell in at least three central planes (excluding the basal and top plane). Costes method
797 was implemented with 100 repetitions to test for statistical significance of colocalisation coefficients
798 (Costes *et al*, 2004).

799

800

801 ## Analysis of patch clamp and Ca^{2+} imaging data

802 Analysis of electrophysiology data and figure preparation was performed using Igor Pro 6 and 7
803 (WaveMetrics Inc.) and final figures were compiled using Adobe Illustrator. For analyzing current
804 density-voltage relations (IVs), the evoked Ca^{2+} current was averaged from 5 to 10 ms after
805 depolarization start. Cells expressing current amplitudes less than -49 pA and with current density
806 greater than -60 pA/pF were not taken into account for analysis.

807 Ca^{2+} imaging data analysis was performed using a customized script in ImageJ. Briefly, we performed
808 background subtraction in time series with Calbryte590 signal and then averaged 5 frames before
809 stimulation and subtracted these from an average of three frames during stimulation to obtain ΔF
810 images. For visualization, the images were smoothened (3 X 3 unweighted smoothening) and a
811 composite was created by overlaying the ΔF images and the RIBEYE-GFP channel. For analyzing $\Delta F/F_0$,
812 we drew circular regions of interest (ROIs) of 2µm diameter at sites with and without *SyRibbons* in the
813 background subtracted time series. The $\Delta F_{max}/F_0$ was calculated as the of average $\Delta F/F_0$ in first three
814 frames of peak Ca^{2+} signal intensity at stimulation onset in each ROI. To minimize bias while assigning
815 regions as with or without *SyRibbons*, ROIs were assigned in the RIBEYE-GFP channel, without looking
816 at the corresponding Calbryte590 signal.

817

818 ## Statistics

819 Data sorting and statistics were performed using MS Excel, *Igor Pro 7* and/or *GraphPad Prism 10*.
820 Numerical data is represented mainly as mean ± standard deviation (SD). The normality of data was
821 assessed using Jarque-Bera test and Kolmogorov-Smirnov test, and the equality of variances was
822 checked using *F*-test. When comparing two samples, a two-tailed unpaired Student's *t*-test (or paired
823 *t*-test for Fig. 7J) was performed for normally distributed samples with equal variances. If the
824 conditions for normality and equality of variances were not met, an unpaired Mann-Whitney-Wilcoxon
825 test was performed. When comparing multiple samples, a one-way ANOVA with post hoc Tukey's test
826 was used for normally distributed data with equal variances. For samples which were not normally
827 distributed, we used Kruskal-Wallis test with *post hoc* Dunn's multi-comparison correction. All box
828 plots are depicted with crosses representing mean values, central bands indicating median, whiskers
829 for 90/10 percentiles, boxes for 75/25 percentiles and individual data points overlaid. Non-significant
830 differences have been indicated as n.s., while significant *P* values have been depicted as $*P$ for < 0.05,
831 $**P < 0.01$, $***P < 0.001$, and $****P < 0.0001$.

832

833

834

835

Acknowledgments:

We would like to thank Dr. Kathrin Kusch for advice on cloning, Dr. Jakob Neef for critical feedback on the manuscript, and Nare Karagulyan for valuable discussions regarding Ca^{2+} imaging. We are grateful to Sandra Gerke, Christiane Senger-Freitag, Sina Langer, Fabienne Hahn and Ina Preuss for expert technical assistance and Patricia Räke-Kügler for the administrative support during this study. We would also like to thank Prof. Erwin Neher and Prof. Silvio Rizzoli for their feedback throughout the course of this study. Lastly, we would like to thank lab rotation students Gantavya Arora and Ugur Coskun for their initial contributions to the project.

Funding:

RK was supported by funding from the Studienstiftung des Deutschen Volkes. This work was further supported by funding of the European Union (ERC, "DynaHear", grant agreement No. 101054467) and Fondation Pour l'Audition (FPA RD-2020-10) to TM and by Deutsche Forschungsgemeinschaft (DFG, German Research Foundation) via the EXC 2067/1 (MBExC) to TM, SEL and RFB. Open access funding provided by Max Planck Society.

Author Contributions: TM and RK designed the study. RK performed the experiments and the analysis under supervision of TM. TTD performed cryo-CLEM experiments under supervision of AP and RFB. TD, NS and SEL prepared and characterized expression plasmids for membrane targeted Bassoon (TD) and EGFP/Halo-tagged $Ca_V1.3\alpha1$ (NS, SEL). RK and TM prepared the manuscript with contribution of all authors.

Disclosure and Competing Interests Statement: The authors declare that no competing interests exist.

References

Ann Marie Craig, Ethan R. Graf, & Michael W. Linhoff (2006) How to build a central synapse: clues from cell culture. *Trends Neurosci* Volume 29: 8–20

Becker L, Schnee ME, Niwa M, Sun W, Maxeiner S, Talaei S, Kachar B, Rutherford MA & Ricci AJ (2018) The presynaptic ribbon maintains vesicle populations at the hair cell afferent fiber synapse. *eLife* 7: e30241

Böhme MA, Beis C, Reddy-Alla S, Reynolds E, Mampell MM, Grasskamp AT, Lützkendorf J, Bergeron DD, Driller JH, Babikir H, *et al* (2016) Active zone scaffolds differentially accumulate Unc13 isoforms to tune Ca^{2+} channel–vesicle coupling. *Nat Neurosci* 19: 1311–1320

Brandt A (2005) Few CaV1.3 Channels Regulate the Exocytosis of a Synaptic Vesicle at the Hair Cell Ribbon Synapse. *J Neurosci* 25: 11577–11585

870 Brandt A, Striessnig J & Moser T (2003) Ca_V 1.3 Channels Are Essential for Development and
871 Presynaptic Activity of Cochlear Inner Hair Cells. *J Neurosci* 23: 10832–10840

872 Bunt AH (1971) Enzymatic digestion of synaptic ribbons in amphibian retinal photoreceptors. *Brain*
873 *Res* 25: 571–577

874 Costes SV, Daelemans D, Cho EH, Dobbin Z, Pavlakis G & Lockett S (2004) Automatic and quantitative
875 measurement of protein-protein colocalization in live cells. *Biophys J* 86: 3993–4003

876 Davydova D, Marini C, King C, Klueva J, Bischof F, Romorini S, Montenegro-Venegas C, Heine M,
877 Schneider R, Schröder MS, *et al* (2014) Bassoon specifically controls presynaptic P/Q-type
878 Ca(2+) channels via RIM-binding protein. *Neuron* 82: 181–194

879 Dick O, tom Dieck S, Altrock WD, Ammermüller J, Weiler R, Garner CC, Gundelfinger ED &
880 Brandstätter JH (2003) The Presynaptic Active Zone Protein Bassoon Is Essential for
881 Photoreceptor Ribbon Synapse Formation in the Retina. *Neuron* 37: 775–786

882 tom Dieck S, Altrock WD, Kessels MM, Qualmann B, Regus H, Brauner D, Fejtová A, Bracko O,
883 Gundelfinger ED & Brandstätter JH (2005) Molecular dissection of the photoreceptor ribbon
884 synapse: physical interaction of Bassoon and RIBEYE is essential for the assembly of the
885 ribbon complex. *J Cell Biol* 168: 825–836

886 tom Dieck S, Sanmartí-Vila L, Langnaese K, Richter K, Kindler S, Soyke A, Wex H, Smalla KH, Kämpf U,
887 Fränzer JT, *et al* (1998) Bassoon, a novel zinc-finger CAG/glutamine-repeat protein selectively
888 localized at the active zone of presynaptic nerve terminals. *J Cell Biol* 142: 499–509

889 tom Dieck S, Specht D, Strenzke N, Hida Y, Krishnamoorthy V, Schmidt K-F, Inoue E, Ishizaki H,
890 Tanaka-Okamoto M, Miyoshi J, *et al* (2012) Deletion of the presynaptic scaffold CAST reduces
891 active zone size in rod photoreceptors and impairs visual processing. *J Neurosci* 32: 12192–
892 12203

893 Dou H, Vazquez AE, Namkung Y, Chu H, Cardell EL, Nie L, Parson S, Shin H-S & Yamoah EN (2004) Null
894 mutation of alpha1D Ca^{2+} channel gene results in deafness but no vestibular defect in mice. *J*
895 *Assoc Res Otolaryngol JARO* 5: 215–226

896 Edmonds BW (2004) Evidence that fast exocytosis can be predominantly mediated by vesicles not
897 docked at active zones in frog saccular hair cells. *J Physiol* 560: 439–450

898 Eisenstein F, Yanagisawa H, Kashihara H, Kikkawa M, Tsukita S & Danev R (2023) Parallel cryo
899 electron tomography on in situ lamellae. *Nat Methods* 20: 131–138

900 Frank T, Khimich D, Neef A & Moser T (2009) Mechanisms contributing to synaptic Ca2+ signals and
901 their heterogeneity in hair cells. *Proc Natl Acad Sci* 106: 4483–4488

902 Frank T, Rutherford MA, Strenzke N, Neef A, Pangršič T, Khimich D, Fejtova A, Gundelfinger ED,
903 Liberman MC, Harke B, *et al* (2010) Bassoon and the synaptic ribbon organize Ca^{2+} channels
904 and vesicles to add release sites and promote refilling. *Neuron* 68: 724–738

905 Glowatzki E & Fuchs PA (2002) Transmitter release at the hair cell ribbon synapse. *Nat Neurosci* 5:
906 147–154

907 Grabner CP, Gandini MA, Rehak R, Le Y, Zamponi GW & Schmitz F (2015) RIM1/2-Mediated
908 Facilitation of Cav1.4 Channel Opening Is Required for Ca2+-Stimulated Release in Mouse
909 Rod Photoreceptors. *J Neurosci* 35: 13133–13147

910 Grabner CP, Jansen I, Neef J, Weihs T, Schmidt R, Riedel D, Wurm CA & Moser T (2022) Resolving the
911 molecular architecture of the photoreceptor active zone with 3D-MINFLUX. *Sci Adv* 8:
912 eabl7560

913 Grabner CP & Moser T (2021) The mammalian rod synaptic ribbon is essential for Cav channel
914 facilitation and ultrafast synaptic vesicle fusion. *eLife* 10: e63844

915 Graydon CW, Cho S, Li G-L, Kachar B & von Gersdorff H (2011) Sharp Ca2+ Nanodomains beneath the
916 Ribbon Promote Highly Synchronous Multivesicular Release at Hair Cell Synapses. *J Neurosci*
917 31: 16637–16650

918 Hagiwara A, Kitahara Y, Grabner CP, Vogl C, Abe M, Kitta R, Ohta K, Nakamura K, Sakimura K, Moser
919 T, *et al* (2018) Cytomatrix proteins CAST and ELKS regulate retinal photoreceptor
920 development and maintenance. *J Cell Biol* 217: 3993–4006

921 Heck J, Parutto P, Ciuraszkiewicz A, Bikbaev A, Freund R, Mitlöhner J, Andres-Alonso M, Fejtova A,
922 Holcman D & Heine M (2019) Transient Confinement of CaV2.1 Ca2+-Channel Splice Variants
923 Shapes Synaptic Short-Term Plasticity. *Neuron* 103: 66-79.e12

924 Heidelberger R, Heinemann C, Neher E & Matthews G (1994) Calcium dependence of the rate of
925 exocytosis in a synaptic terminal. *Nature* 371: 513–515

926 Hibino H, Pironkova R, Onwumere O, Vologodskaia M, Hudspeth AJ & Lesage F (2002) RIM - binding
927 proteins (RBPs) couple Rab3 - interacting molecules (RIMs) to voltage - gated Ca2+ channels.
928 *Neuron* 34: 411–423

929 Holt M, Cooke A, Neef A & Lagnado L (2004) High Mobility of Vesicles Supports Continuous
930 Exocytosis at a Ribbon Synapse. *Curr Biol* 14: 173–183

931 Inoue E, Deguchi-Tawarada M, Takao-Rikitsu E, Inoue M, Kitajima I, Ohtsuka T & Takai Y (2006) ELKS,
932 a protein structurally related to the active zone protein CAST, is involved in Ca2+-dependent
933 exocytosis from PC12 cells. *Genes Cells* 11: 659–672

934 Jaime Tobón LM & Moser T (2023) Ca2+ regulation of glutamate release from inner hair cells of
935 hearing mice. *Proc Natl Acad Sci* 120: e2311539120

936 Jarsky T, Tian M & Singer JH (2010) Nanodomain control of exocytosis is responsible for the signaling
937 capability of a retinal ribbon synapse. *J Neurosci Off J Soc Neurosci* 30: 11885–11895

938 Jean P, Morena DL de la, Michanski S, Tobón LMJ, Chakrabarti R, Picher MM, Neef J, Jung S, Gültas M,
939 Maxeiner S, *et al* (2018) The synaptic ribbon is critical for sound encoding at high rates and
940 with temporal precision. *eLife* 7: e29275

941 Jing Z, Rutherford MA, Takago H, Frank T, Fejtova A, Khimich D, Moser T & Strenzke N (2013)
942 Disruption of the presynaptic cytomatrix protein bassoon degrades ribbon anchorage,
943 multiquantal release, and sound encoding at the hair cell afferent synapse. *J Neurosci* 33:
944 4456–4467

945 Jung S, Oshima-Takago T, Chakrabarti R, Wong AB, Jing Z, Yamanbaeva G, Picher MM, Wojcik SM,
946 Göttfert F, Predoehl F, *et al* (2015) Rab3-interacting molecules 2α and 2β promote the
947 abundance of voltage-gated CaV1.3 Ca2+ channels at hair cell active zones. *Proc Natl Acad*
948 *Sci* 112: E3141–E3149

949 Kaeser PS, Deng L, Wang Y, Dulubova I, Liu X, Rizo J & Südhof TC (2011) RIM proteins tether Ca2+
950 channels to presynaptic active zones via a direct PDZ-domain interaction. *Cell* 144: 282–295

951 Khimich D, Nouvian R, Pujol R, tom Dieck S, Egner A, Gundelfinger ED & Moser T (2005) Hair cell
952 synaptic ribbons are essential for synchronous auditory signalling. *Nature* 434: 889–894

953 Krinner S, Butola T, Jung S, Wichmann C & Moser T (2017) RIM-Binding Protein 2 Promotes a Large
954 Number of CaV1.3 Ca2+-Channels and Contributes to Fast Synaptic Vesicle Replenishment at
955 Hair Cell Active Zones. *Front Cell Neurosci* 11: 334

956 Krinner S, Predoehl F, Burfeind D, Vogl C & Moser T (2021) RIM-Binding Proteins Are Required for
957 Normal Sound-Encoding at Afferent Inner Hair Cell Synapses. *Front Mol Neurosci* 14: 651935

958 Liberman MC (1980) Morphological differences among radial afferent fibers in the cat cochlea: an
959 electron-microscopic study of serial sections. *Hear Res* 3: 45–63

960 Liu KSY, Siebert M, Mertel S, Knoche E, Wegener S, Wichmann C, Matkovic T, Muhammad K, Depner
961 H, Mettke C, *et al* (2011) RIM-binding protein, a central part of the active zone, is essential
962 for neurotransmitter release. *Science* 334: 1565–1569

963 Luo F, Liu X, Südhof TC & Acuna C (2017) Efficient stimulus-secretion coupling at ribbon synapses
964 requires RIM-binding protein tethering of L-type Ca^{2+} channels. *Proc Natl Acad Sci* 114:
965 E8081–E8090

966 Magupalli VG, Schwarz K, Alpadi K, Natarajan S, Seigel GM & Schmitz F (2008) Multiple RIBEYE-RIBEYE
967 interactions create a dynamic scaffold for the formation of synaptic ribbons. *J Neurosci Off J*
968 *Soc Neurosci* 28: 7954–7967

969 Mastronarde DN (1997) Dual-Axis Tomography: An Approach with Alignment Methods That Preserve
970 Resolution. *J Struct Biol* 120: 343–352

971 Matthews G & Fuchs P (2010) The diverse roles of ribbon synapses in sensory neurotransmission. *Nat*
972 *Rev Neurosci* 11: 812–822

973 Maxeiner S, Luo F, Tan A, Schmitz F & Südhof TC (2016) How to make a synaptic ribbon: RIBEYE
974 deletion abolishes ribbons in retinal synapses and disrupts neurotransmitter release. *EMBO J*
975 35: 1098–1114

976 Mehta B, Snellman J, Chen S, Li W & Zenisek D (2013) Synaptic Ribbons Influence the Size and
977 Frequency of Miniature-like Evoked Postsynaptic Currents. *Neuron* 77: 516–527

978 Michanski S, Kapoor R, Steyer AM, Möbius W, Früholz I, Ackermann F, Gültas M, Garner CC, Hamra
979 FK, Neef J, *et al* (2023) Piccolino is required for ribbon architecture at cochlear inner hair cell
980 synapses and for hearing. *EMBO Rep* 24: e56702

981 Michanski S, Smaluch K, Steyer AM, Chakrabarti R, Setz C, Oestreicher D, Fischer C, Möbius W, Moser
982 T, Vogl C, *et al* (2019) Mapping developmental maturation of inner hair cell ribbon synapses
983 in the apical mouse cochlea. *Proc Natl Acad Sci* 116: 6415–6424

984 Moser T, Grabner CP & Schmitz F (2019) Sensory processing at ribbon synapses in the retina and the
985 cochlea. *Physiol Rev* 100: 103–144

986 Moser T, Karagulyan N, Neef J & Jaime Tobón LM (2023) Diversity matters — extending sound
987 intensity coding by inner hair cells via heterogeneous synapses. *EMBO J* 42: e114587

988 Müller TM, Gierke K, Joachimsthaler A, Sticht H, Izsvák Z, Hamra FK, Fejtová A, Ackermann F, Garner
989 CC, Kremers J, *et al* (2019) A multiple Piccolino-RIBEYE interaction supports plate-shaped
990 synaptic ribbons in retinal neurons. *J Neurosci* 39: 2038–18

991 Naoum P. Issa & A. J. Hudspeth (1996) Characterization of fluo-3 labelling of dense bodies at the hair
992 cell's presynaptic active zone. *J Neurocytol* 25: 257–266

993 Neef J, Urban NT, Ohn T-L, Frank T, Jean P, Hell SW, Willig KI & Moser T (2018) Quantitative optical
994 nanophysiology of Ca^{2+} signaling at inner hair cell active zones. *Nat Commun* 9: 290

995 Ohn T-L, Rutherford MA, Jing Z, Jung S, Duque-Afonso CJ, Hoch G, Picher MM, Scharinger A, Strenzke
996 N & Moser T (2016) Hair cells use active zones with different voltage dependence of Ca^{2+}
997 influx to decompose sounds into complementary neural codes. *Proc Natl Acad Sci* 113:
998 E4716–E4725

999 Ohtsuka T, Takao-Rikitsu E, Inoue E, Inoue M, Takeuchi M, Matsubara K, Deguchi-Tawarada M, Satoh
1000 K, Morimoto K, Nakanishi H, *et al* (2002) Cast: a novel protein of the cytomatrix at the active
1001 zone of synapses that forms a ternary complex with RIM1 and munc13-1. *J Cell Biol* 158: 577–
1002 590

1003 Özçete ÖD & Moser T (2021) A sensory cell diversifies its output by varying Ca^{2+} influx-release
1004 coupling among active zones. *EMBO J* 40: e106010

1005 Park D, Wu Y, Lee S-E, Kim G, Jeong S, Milovanovic D, Camilli PD & Chang S (2021) Cooperative
1006 function of synaptophysin and synapsin in the generation of synaptic vesicle-like clusters in
1007 non-neuronal cells. *Nat Commun* 12

1008 Picher MM, Gehrt A, Meese S, Ivanovic A, Predoehl F, Jung S, Schrauwen I, Dragonetti AG, Colombo
1009 R, Camp GV, *et al* (2017a) Ca2+-binding protein 2 inhibits Ca2+-channel inactivation in mouse
1010 inner hair cells. *Proc Natl Acad Sci* 114: E1717–E1726

1011 Picher MM, Oprişoreanu A-M, Jung S, Michel K, Schoch S & Moser T (2017b) Rab Interacting
1012 Molecules 2 and 3 Directly Interact with the Pore-Forming CaV1.3 Ca2+ Channel Subunit and
1013 Promote Its Membrane Expression. *Front Cell Neurosci* 11

1014 Pierson JA, Yang JE & Wright ER (2024) Recent advances in correlative cryo-light and electron
1015 microscopy. *Curr Opin Struct Biol* 89: 102934

1016 Platzer J, Engel J, Schrott-Fischer A, Stephan K, Bova S, Chen H, Zheng H & Striessnig J (2000)
1017 Congenital deafness and sinoatrial node dysfunction in mice lacking class D L-type Ca^{2+}
1018 channels. *Cell* 102: 89–97

1019 Rigort A, Bäuerlein FJB, Leis A, Gruska M, Hoffmann C, Laugks T, Böhm U, Eibauer M, Gnaegi H,
1020 Baumeister W, *et al* (2010) Micromachining tools and correlative approaches for cellular
1021 cryo-electron tomography. *J Struct Biol* 172: 169–179

1022 Robertis ED & Franchi CM (1956) Electron Microscope Observations on Synaptic Vesicles in Synapses
1023 of the Retinal Rods and Cones. *J Biophys Biochem Cytol* 2: 307–318

1024 Rohou A & Grigorieff N (2015) CTFFIND4: Fast and accurate defocus estimation from electron
1025 micrographs. *J Struct Biol* 192: 216–221

1026 Sakamoto H, Ariyoshi T, Kimpara N, Sugao K, Taiko I, Takikawa K, Asanuma D, Namiki S & Hirose K
1027 (2018) Synaptic weight set by Munc13-1 supramolecular assemblies. *Nat Neurosci* 21: 41–49

1028 Schindelin J, Arganda-Carreras I, Frise E, Kaynig V, Longair M, Pietzsch T, Preibisch S, Rueden C,
1029 Saalfeld S, Schmid B, *et al* (2012) Fiji: an open-source platform for biological-image analysis.
1030 *Nat Methods* 9: 676–682

1031 Schmitz F, Königstorfer A & Südhof TC (2000) RIBEYE, a component of synaptic ribbons: a protein's
1032 journey through evolution provides insight into synaptic ribbon function. *Neuron* 28: 857–
1033 872

1034 Schwenzer N, Tsukanov R, Kohl T, Basak S, Seibertz F, Voigt N, Enderlein J & Lehnart SE (2024)
1035 Nanoscale architecture and dynamics of CaV1.3 channel clusters in cardiac myocytes
1036 revealed by single channel nanoscopy. *bioRxiv*

1037 Singer JH, Lassová L, Vardi N & Diamond JS (2004) Coordinated multivesicular release at a
1038 mammalian ribbon synapse. *Nat Neurosci* 7: 826–833

1039 Smith CA & Sjöstrand FS (1961) A synaptic structure in the hair cells of the guinea pig cochlea. *J*
1040 *Ultrastruct Res* 5: 184–192

1041 Snellman J, Mehta B, Babai N, Bartoletti TM, Akmentin W, Francis A, Matthews G, Thoreson W &
1042 Zenisek D (2011) Acute destruction of the synaptic ribbon reveals a role for the ribbon in
1043 vesicle priming. *Nat Neurosci* 14: 1135–1141

1044 Sobkowicz H, Rose J, Scott G & Slapnick S (1982) Ribbon synapses in the developing intact and
1045 cultured organ of Corti in the mouse. *J Neurosci* 2: 942–957

1046 Stamataki S, Francis HW, Lehar M, May BJ & Ryugo DK (2006) Synaptic alterations at inner hair cells
1047 precede spiral ganglion cell loss in aging C57BL/6J mice. *Hear Res* 221: 104–118

1048 Sternberg (1983) Biomedical Image Processing. *Computer* 16: 22–34

1049 Vaithianathan T, Henry D, Akmentin W & Matthews G (2016) Nanoscale dynamics of synaptic vesicle
1050 trafficking and fusion at the presynaptic active zone. *eLife* 5: e13245

1051 Wichmann C & Kuner T (2022) Heterogeneity of glutamatergic synapses: cellular mechanisms and
1052 network consequences. *Physiol Rev* 102: 269–318

1053 Wichmann C & Moser T (2015) Relating structure and function of inner hair cell ribbon synapses. *Cell*
1054 *Tissue Res*

1055 Wong AB, Rutherford MA, Gabrielaitis M, Pangršič T, Göttfert F, Frank T, Michanski S, Hell S, Wolf F,
1056 Wichmann C, *et al* (2014) Developmental refinement of hair cell synapses tightens the
1057 coupling of Ca2+ influx to exocytosis. *EMBO J* 33: 247–264

1058 Zheng SQ, Palovcak E, Armache J-P, Verba KA, Cheng Y & Agard DA (2017) MotionCor2: anisotropic
1059 correction of beam-induced motion for improved cryo-electron microscopy. *Nat Methods* 14:
1060 331–332

1061